Impacts of Numerical Advection Schemes and Turbulence Modeling on Gray-Zone Simulation of a Squall Line

JIANAN CHEN[a] AND XIAOMING SHI[a,b]

[a] Hong Kong University of Science and Technology, Hong Kong, China
[b] Center for Ocean Research in Hong Kong and Macau, Hong Kong University of Science and Technology, Hong Kong, China

(Manuscript received 22 August 2024, in final form 20 February 2025, accepted 6 March 2025)

ABSTRACT: With increasing computational power, atmospheric simulations have approached the gray-zone resolutions, where energetic turbulent eddies are partly resolved. The representation of turbulence in the gray zone is challenging and sensitive to the choices of turbulence models and numerical advection schemes. Numerical advection schemes are typically designed with numerical dissipation to suppress small-scale numerical oscillations. However, at gray-zone resolutions, the numerical dissipation can damp both numerical and physical oscillations. In this study, we first evaluate the impact of advection schemes on the simulation of an idealized squall line at two gray-zone resolutions (1 and 4 km). We found that at the 4-km resolution, the numerical dissipation from advection schemes can be unfavorable because it damps convective cells greatly and weakens the front-to-rear flow, producing an underestimated convective precipitation maximum and excessive stratiform precipitation. At the 1-km resolution, the numerical dissipation is essential because, without it, excessive spurious numerical oscillations disrupt the squall-line structure. The dynamic reconstruction model (DRM) of turbulence is designed to model both forward- and backscatter having the potential to counter the effect of numerical dissipation from the advection schemes. Our findings demonstrate that DRM enhances squall-line simulations at the 4-km resolution, improving both the squall-line structure and precipitation distribution. However, at the 1-km resolution, DRM fails to improve simulation accuracy, likely due to its influence on triggering spurious convections.

SIGNIFICANCE STATEMENT: This work investigates the effects of numerical mixing arising from numerical advection schemes and physical mixing from turbulence schemes on an organized deep convective system in the gray zone. The numerical mixing is found to be critical in shaping the deep convective system structure and the corresponding precipitation distribution. Meanwhile, the role of numerical mixing varies with gray-zone resolutions. The numerical mixing is necessary when it primarily acts on spurious numerical oscillations but unfavorable when it mainly acts on physical convections. Turbulence schemes that allow backscatter can reduce the impact of numerical mixing, which helps improve the accuracy of simulations at certain gray-zone resolutions.

KEYWORDS: Cloud resolving models; Parameterization; Subgrid-scale processes

1. Introduction

Subgrid-scale (SGS) turbulence mixing is important for convection-permitting simulations because of its vital role in transporting momentum, heat, and other scalars (Honnert et al. 2020). With increasing computational power, grid resolutions have reached the kilometer scale, which is in the gray zone for convection (Chow et al. 2019). In the mesoscale simulations at resolutions far coarser than the kilometer scale, the subgrid turbulence mixing is parameterized using one-dimensional planetary boundary layer (PBL) schemes under the assumption that turbulence is unresolved (Chow et al. 2019; Shi et al. 2019). In large-eddy simulations (LESs) with grid spacing far smaller than the kilometer scale, the subgrid turbulence mixing is parameterized using three-dimensional turbulence closure models under the assumption that the energy-containing eddies are resolved (Shi et al. 2019). However, neither of these assumptions fit in the gray-zone simulations, where the energy-containing eddies are partly resolved. The challenge in gray-zone simulations is confronted at two main directions: either through improving the PBL schemes (e.g., Shin and Hong 2015) or adapting the LES turbulence models (e.g., Parodi and Tanelli 2010). The direction of implementing LES-type closure has demonstrated promising performance (Chow et al. 2019). In this study, we focus exclusively on LES-type turbulence modeling.

In addition to the explicit mixing due to subgrid turbulence schemes, the implicit mixing (i.e., numerical dissipation and dissipation) due to numerical advection schemes is also of significant importance in gray-zone simulations (Beare 2014). Previous research suggests that numerical dissipation affects convective cells more than the explicit mixing from subgrid turbulence scheme in gray-zone resolutions of squall-line simulations (Weisman et al. 1997). The numerical dissipation of advection schemes is due to the truncation errors that are formulated as a diffusive operator (Durran 2010). In numerical simulations, numerical dissipation has a critical role in damping spurious numerical oscillations that are often caused by computing the high-order approximations using the grid points near

Supplemental information related to this paper is available at the Journals Online website: https://doi.org/10.1175/MWR-D-24-0174.s1.

Corresponding author: Xiaoming Shi, shixm@ust.hk

DOI: 10.1175/MWR-D-24-0174.1

sharp gradients (Borges et al. 2008). Sharp gradients are ubiquitous in atmospheric simulations, such as the thermodynamic processes associated with the moisture and temperature discontinuities (Wang et al. 2021).

Advection schemes are categorized as odd-order or even-order based on the type of difference approximation used for the spatial derivatives. Even-order schemes use central differencing approximations, while odd-order schemes typically use upwind approximations (Kusaka et al. 2005). Different from odd-order schemes, which have inherent numerical dissipation, even-order schemes have no numerical dissipation (Durran 2010). Without numerical dissipation, spurious numerical oscillations may develop into grid-scale convections. As a result, an even-order advection scheme typically needs an extra artificial dissipation term with coefficients that are specified empirically (Durran 2010; Xue 2000). The odd-order schemes, such as the fifth-order advection scheme (ODD5) and the fifth-order weighted essentially nonoscillatory (WENO5) scheme, are popularly used schemes in atmospheric models such as WRF (Skamarock et al. 2008) and Cloud Model 1 (Bryan and Fritsch 2002), probably because they are advantageous combinations of computational efficiency and accuracy. In addition, there is no need to specify an extra numerical dissipation term which is needed in the even-order scheme. Compared with ODD5, the WENO5 is often viewed as a more advanced advection scheme, which gives nonoscillatory solutions by increasing the numerical dissipation near the sharp gradient (Jiang and Shu 1996; Pressel et al. 2015). It has been shown that the increased implicit numerical dissipation of the WENO5 scheme is beneficial in damping the grid-scale erroneous convections and reducing spurious numerical oscillations (Pressel et al. 2015; Bryan 2005). The WENO schemes are also recommended in coarser-resolution simulations because fewer numerical oscillations are induced (Pressel et al. 2015; Wang et al. 2021).

Nonetheless, the numerical dissipation of advection schemes is not always beneficial. For example, the numerical dissipation from the WENO scheme has been found to suppress the energy cascade in turbulence-resolving simulations and subsequently lead to unsatisfactory predictions of turbulence characteristics (Wang et al. 2021). Different from the mixing due to subgrid turbulence schemes, which are physically based, the numerical dissipation acts on small-scale motions indiscriminately (Takemi and Rotunno 2003). Not only the unphysical, spurious numerical oscillations but also physical, realistic perturbations related to the instability growth are impacted by the numerical dissipation. To leverage the benefits of even-order and odd-order schemes, hybrid advection schemes that combine odd-order and even-order schemes have been developed and have shown improved performance in maintaining numerical stability and reducing numerical dissipation (Kosović et al. 2016). In the gray-zone simulations where grid size is close to the scale of energy-containing eddies (Chow et al. 2019), the numerical dissipation from the advection scheme may consume energy-containing eddies. Weisman et al. (1997) have found that increased numerical dissipation smooths the convective cells in squall simulations. However, the impact of numerical dissipation from advection schemes on the overall structure of squall lines has not been evaluated in gray-zone resolutions. The first aim of this study is to evaluate the impact of numerical advection schemes on gray-zone simulations of squall lines. In particular, we focus on how the numerical diffusion in advection schemes can affect the squall-line organization and precipitation distribution.

Traditional turbulence closure models are dissipative, in which the momentum or scalar can only be transferred from larger (resolved) scales to smaller (subgrid) scales (Chow et al. 2019). This assumption is acceptable at LES resolutions, where subgrid-scale motions are within the inertial subrange and mostly dissipative (e.g., Honnert et al. 2020; Sun et al. 2021). In the gray zone, the subgrid-scale motions are not dissipative. By filtering the high-resolution LES to the gray-zone resolutions, previous research has found a significant amount of backscatter of momentum in gray-zone simulations of squall lines (Lai and Waite 2020) and supercells (Sun et al. 2021).

Subgrid mixing models that allow backscatter have been advocated in the gray-zone simulations (Chow et al. 2019). The dynamic reconstruction model (DRM) is one of such models that allows backscattering. It uses an explicit filtering and reconstruction framework to reduce numerical error from the grid discretization (Gullbrand and Chow 2003), which enhances the fidelity of the resolved field (Chow et al. 2005). Previous research has found the DRM has significantly improved the turbulent motion in neutral boundary layers (Chow et al. 2005), the convective boundary layer (Simon et al. 2019), the stratocumulus-capped boundary layer (Shi et al. 2018a,b), and deep tropical convection (Shi et al. 2019). The dependence on grid resolution in the gray-zone simulation has been significantly reduced. In addition, the DRM can better simulate deep tropical convection in 1-km-resolution simulations regarding domain-wide characteristics such as the domainwide precipitation amount, the distribution of clouds, and vertical fluxes (Shi et al. 2019). However, the impact of the DRM on organized deep convective systems has not been assessed. The second aim, in our study, is to evaluate the performance of the DRM in simulating the squall line.

This paper will detail the numerical model, different turbulence schemes, and advection schemes in section 2. Section 3 describes the results of the benchmark simulation. The impacts of implicit (inherently from an odd-order scheme) and explicit numerical dissipation (used with an even-order scheme) on squall-line simulations are explored in sections 4 and 5, respectively. The performance of the DRM is evaluated in section 6. A summary and conclusions are provided in section 7.

2. Simulation methods and model configurations

In this section, we outline the key simulation methodologies and model configurations used in our study, with focuses on 1) turbulence closure schemes, 2) advection schemes, and 3) numerical model setup.

a. Turbulence closure schemes

In large-eddy simulations, turbulence closure is used to model subgrid motions. The grid mesh separates the subgrid-scale motion and the motion larger than the grid. However, due to the grid discretization and the discrete differentiation operation, only the motions larger than the model's effective resolution (typically larger than $6\Delta x$ for advection schemes with six-order dissipation) can be resolved (Chow et al. 2005). The turbulent motions are divided into resolved and subfilter scale (SFS). The modeling of SFS turbulence differs between closure models (Shi et al. 2018b). In this study, we mainly compare two closure models. One is a traditional LES closure, the 1.5-order turbulent kinetic energy (TKE) scheme (Moeng 1984; Deardorff 1980), with no backscattering allowed. The other is the DRM (Chow et al. 2005), which permits the backscatter.

1) 1.5-order TKE model

The 1.5-order TKE model is a traditional LES closure with the eddy-viscosity-based form (Deardorff 1980). The deviatoric SFS momentum flux is formulated as

$$\tau_{ij} = -2K_m\overline{S_{ij}}, \tag{1}$$

where K_m is the eddy viscosity and $\overline{S_{ij}}$ is the resolved turbulent strain tensor. The SFS scalar flux is similarly formulated as

$$\tau_{\theta j} = -K_h\frac{\partial\overline{\varphi}}{\partial x_j}, \tag{2}$$

where K_h is the eddy diffusivity and $\overline{\varphi}$ represents a scalar variable. The K_h and K_m are determined by the SFS TKE [for details, see Eqs. (7) and (8) in Shi et al. 2018b] that are predicted by a prognostic equation (Moeng 1984). The key assumption of this closure method is that the resolved turbulence generates downgradient fluxes and transfers its energy and scalar variance to smaller turbulences.

2) Dynamic reconstruction model

The DRM is a more advanced turbulence closure model that partitions the SFS fluxes into resolvable SFS (RSFS) and SGS components. The RSFS refers to the turbulent motion scales larger than the explicit filter but smaller than the effective resolution (Chow et al. 2005). The turbulent motions in the RSFS are partly resolved and able to produce countergradient fluxes in gray-zone simulations (Chow et al. 2005). In the traditional LES closure, the SFS and resolved motions are divided through the implicit filter, which can differ for each term in the equations, making the reconstruction of RSFS impossible (Chow et al. 2005). In contrast, the DRM defines and applies an explicit filter enabling the reconstruction of RSFS. The approximate deconvolution method is employed to reconstruct the RSFS stress (Stolz and Adams 1999). The velocity field is constructed by the following equation:

$$\tilde{u}_i = \overline{\tilde{u}_i} + (\mathbf{I}-\mathbf{G})*\overline{\tilde{u}}_i + (\mathbf{I}-\mathbf{G})*[(\mathbf{I}-\mathbf{G})*\overline{\tilde{u}_i}] + \cdots, \tag{3}$$

where $\mathbf{G}$ is an explicit filter, $\mathbf{I}$ is the identity operator, the asterisk sign on the right-hand side of the equation represents the convolution operator, the grid discretization is represented by the tilde sign, and the effect of the explicit filter is represented by the overbar sign. The reconstruction level is defined by the number of terms used on the right side of the equation. The reconstruction of the nth level maintains the initial $n + 1$ terms on the right-hand side. A higher level of reconstruction allows the velocity field to be better reconstructed (Simon et al. 2019). However, the DRM shows diminishing improvement with increased order (Shi et al. 2018b). The high level of reconstruction in the gray zone involves the use of more grid cells for reconstruction and may introduce spurious mixing (Shi et al. 2018b). Here, we consider level two and level zero reconstruction, referred to as DRM0 and DRM2. DRM2 is expected to have larger RSFS contributions than DRM0 due to the higher level of reconstruction. The SFS stress in DRM is formulated as

$$\tau_{ij} = -2K_m\overline{S}_{ij} + (\overline{\tilde{u}_i^\star\tilde{u}_j^\star} - \overline{\tilde{u}_i^\star}\,\overline{\tilde{u}_j^\star}), \tag{4}$$

and the SFS flux is formulated as

$$\tau_{\varphi j} = -K_h\frac{\partial\overline{\varphi}}{\partial x_j} + (\overline{\tilde{\varphi}^\star\tilde{u}_j^\star} - \overline{\tilde{\varphi}^\star}\,\overline{\tilde{u}_j^\star}), \tag{5}$$

where u and φ represent the velocities and a scalar variable, respectively, and the star denotes the reconstructed variables. The eddy viscosity coefficient K_m is calculated using a dynamic eddy-viscosity procedure described in Chow et al. (2005) who adopted the method developed by Wong and Lilly (1994). The eddy diffusivity K_h is calculated simply by specifying a turbulent Prandtl number (Pr_t), $K_h = K_m/\mathrm{Pr}_t$, where Pr_t is 1/3.

b. Advection schemes

Considering the advection equation in one dimension, the tendency of a variable ϕ in Cloud Model 1 (CM1) is computed as

$$\frac{\partial(\phi)}{\partial t} = -\frac{\partial(U\phi)}{\partial x}, \tag{6a}$$

$$-\frac{\partial(U\phi)}{\partial x}\bigg|_{x=x_i} = -\frac{1}{\Delta x}[U_{i+(1/2)}\phi_{i+(1/2)} - U_{i-(1/2)}\phi_{i-(1/2)}]$$

$$= -\frac{1}{\Delta x}[F_{i+(1/2)} - F_{i-(1/2)}], \tag{6b}$$

where $F_{i\pm(1/2)}$ is the flux at the face of the grid cell. The Arakawa-C staggered grid (Arakawa and Lamb 1977) is the only grid system considered in this study.

1) The sixth-order scheme

The sixth-order advection scheme uses centered sixth-order differencing. The $\phi_{i-1/2}$ is approximated with six filtered grid values as follows:

$$\phi^{\mathrm{sixth}}_{i-(1/2)} = \frac{1}{60}(\phi_{i-3} - 8\phi_{i-2} + 37\phi_{i-1} + 37\phi_i - 8\phi_{i+1} + \phi_{i+2}). \tag{7}$$

The centered difference scheme has no numerical dissipation, which is therefore prone to numerical instabilities and spurious numerical oscillations (Pressel et al. 2015). An additional explicit artificial dissipation term is often added to the centered advection scheme to remove the shortest waves, and long waves are relatively uninfluenced (Durran 2010).

2) THE FIFTH-ORDER SCHEME

Different from the sixth-order scheme, the fifth-order scheme has implicit numerical dissipation. The $\phi_{i-(1/2)}$ of the fifth order is computed as (Wicker and Skamarock 2002)

$$\phi_{i-(1/2)}^{\text{fifth}} = \frac{1}{60}(2\phi_{i-3} - 13\phi_{i-2} + 47\phi_{i-1} + 27\phi_i - 3\phi_{i+1}). \quad (8)$$

Indeed, $\phi_{i-(1/2)}$ of the fifth order is equivalent to the sum of $\phi_{i-(1/2)}$ of the sixth order and a sixth-order dissipation term (Wicker and Skamarock 2002):

$$\phi_{i-(1/2)}^{\text{fifth}} = \phi_{i-(1/2)}^{\text{sixth}} + \frac{1}{60}(\phi_{i-3} - 5\phi_{i-2} + 10\phi_{i-1} - 10\phi_i + 5\phi_{i+1} - \phi_{i+2}). \quad (9)$$

3) THE FIFTH-ORDER WENO SCHEME

The fifth-order WENO scheme improves the fifth-order advection scheme near the sharp gradient (Jiang and Shu 1996). In the fifth-order scheme, the five grid points can be separated into three stencils. The $\phi_{i-(1/2)}$ can be approximated by each stencil S (Jiang and Shu 1996) as follows:

$$\phi_{i-(1/2)}^{(S=0)} = \frac{1}{6}(2\phi_{i-3} - 7\phi_{i-2} - \phi_{i-1}), \quad (10a)$$

$$\phi_{i-(1/2)}^{(S=1)} = \frac{1}{6}(-\phi_{i-2} + 5\phi_{i-1} + 2\phi_i), \quad (10b)$$

$$\phi_{i-(1/2)}^{(S=2)} = \frac{1}{6}(2\phi_{i-1} + 5\phi_i - \phi_{i+1}). \quad (10c)$$

The linear combination of the three stencils gives the fifth-order approximation:

$$\phi_{i-(1/2)} = w_0\phi_{i-(1/2)}^{(S=0)} + w_1\phi_{i-(1/2)}^{(S=1)} + w_2\phi_{i-(1/2)}^{(S=2)}, \quad (11)$$

which is the same as Eq. (8) when $w_0 = 1/10$, $w_1 = 3/5$, and $w_2 = 1/10$. The WENO scheme maintains fifth-order accuracy in the smooth region and nonoscillatory behavior near the sharp gradient by assigning nonlinear weights to each stencil based on a smoothness indicator (Jiang and Shu 1996). When a stencil encounters a sharp gradient, the stencil will be assigned to a smaller weight. This weighting strategy leads to a smoothing effect near the sharp gradient and can suppress the generation of numerical oscillations. CM1 applies an improved version called WENO-Z (Borges et al. 2008). The details of the smoothness indicator are documented in Borges et al. (2008).

c. *Numerical models and setup*

The model used is the Cloud Model 1, a state-of-the-art atmospheric model that can solve the nonhydrostatic, compressible equations of the moist atmosphere (Bryan and Fritsch 2002). In this study, we use three different horizontal grid spacings: 200 m, 1 km, and 4 km. The domain dimensions are 96 km (Y) × 640 km (X) × 25 km (Z) for the 200-m and 1-km resolution simulations. For the squall-line simulations, the 200-m grid spacing is typically within the LES resolutions where the inertial subrange can be resolved (Bryan and Morrison 2012; Bryan et al. 2003; Lai and Waite 2020). The 1- and 4-km grid spacings are within the gray-zone resolutions of the squall-line simulation. The mesoscale structures of squall lines are resolved in the 1- and 4-km simulations, but the energy peak is not resolved, and substantial subgrid turbulence kinetic energy exists in these resolutions (Weisman et al. 1997; Bryan et al. 2003). For the 4-km resolution simulations, we enlarge the domain with the size of 240 km (Y) × 640 km (X) × 25 km (Z). Domains of all simulations in this study are not translated. A Rayleigh damper is applied at vertical levels above 20 km. The vertical grid size for the 1- and 4-km simulations stretches from 100 m at low levels to 500 m at high levels. For the 200-m simulations, the grid size stretches from 50 m at low levels to 100 m at high levels. The results presented in this study are not sensitive to the vertical grid spacings. A periodic boundary condition is used in the Y direction, while an open boundary is used in the X direction. Free-slip (semislip) conditions are specified for the upper (bottom) boundaries. The surface model uses the original CM1 formulation (Bryan 2012). Following Bryan et al. (2003), we did not apply the large-scale pressure gradient. The Coriolis force is neglected because of the relatively short simulation hours (6 h). The microphysics scheme is the Morrison scheme (Morrison et al. 2009).

The model is integrated up to 6 h when the squall-line cold outflow boundary is still within the computational domain. Following Lai and Waite (2020), the input wind profile (Fig. 1) is based on a classic weak shear case (Weisman and Rotunno 2004) but subtracting a mean wind speed of 10 m s^{-1} from the original weak shear wind profile. This is to ensure that the simulated squall lines are far away from the open boundary during the simulation period. The other sounding profiles are the same as the profiles used in Weisman and Rotunno (2004). The squall line is initiated using a 2-km-deep cold pool where the maximum potential temperature perturbation is set at the surface with −8 K. The initiated cold pool is infinite in the Y direction and extends 80 km from the left boundary (in the X direction). Random temperature perturbations (±0.2 K) are added to the lowest levels to allow the generation of three-dimensional perturbations along the squall line. In the simulations, after the model's spinup, the domain-wide rain rate of the simulations gradually levels off. The last 2 h are viewed as a steady-state period and used for steady-state analysis.

Numerical dissipation comes from both temporal and spatial grid discretization. For the time integration, all simulations use the same split-explicit Runge–Kutta scheme (Wicker and Skamarock 2002). For the spatial discretization, the simple ODD5, WENO5, and centered sixth-order scheme (EVEN6) are used. This study adds no explicit dissipation for WENO5 and ODD5 because of implicit numerical dissipation in the schemes themselves. The vertical and horizontal directions are applied with the same advection scheme for each experiment. For WENO5, it is applied to both scalar and momentum advection.

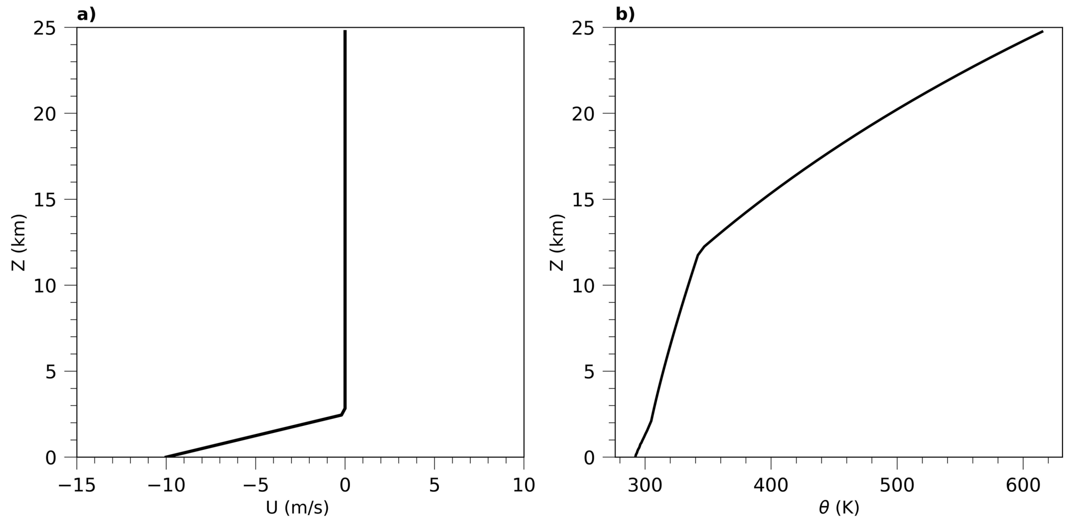

FIG. 1. Vertical profile of horizontal wind in the X direction U (m s^{-1}) and potential temperature θ (K).

In CM1, the sixth-order explicit artificial dissipation is applied with the EVEN6 scheme. The corresponding equation is formulated as $\partial\phi/\partial t = S + \alpha\nabla^6\phi$, where α is the dissipation coefficient and S represents the tendency due to the other terms including advection. The α is further determined by a dissipation parameter β, $\alpha = 2^{-6}\Delta t^{-1}p^{-1}\beta$, where Δt represents the time step and p represents the number of passes of the diffusion scheme (Knievel et al. 2007). The recommended dissipation parameter β for sixth-order dissipation ranges from 0.02 to 0.24. However, these are empirical values. To explore a broader spectrum, we considered a minimum numerical dissipation case ($\beta = 0$), in which no explicit dissipation is applied. In addition, this study uses a simple flux-limited monotonic diffusion scheme (Xue 2000).

The numerical simulations conducted in this study are listed in Table 1. First, we evaluate the impact of implicit numerical dissipation in the WENO5 and ODD5 on the squall-line simulation. Second, the impact of numerical dissipation on the squall-line structure is further investigated using EVEN6 with various degrees of artificial dissipation. Last, the DRMs, in replacement of TKE, are evaluated with different advection schemes.

3. Benchmark simulation

In squall-line simulations, the 200-m grid size falls within the LES resolutions. In this study, the 200-m resolution simulation using the WENO5 advection scheme and TKE turbulence scheme is employed as the benchmark simulation. The squall line at the end of the simulation (at the 6 h) using the WENO5 is shown in Fig. 2a. Consistent with previous studies (e.g., Rotunno et al. 1988), the simulation captures the upshear-tilted squall-line structure characterized by the upshear-tilted convective clouds and well-developed anvil clouds. The steady-state precipitation distribution in the cross-squall-line direction is shown in Fig. 3. The leading edge of the cold pool is normalized to the same location before averaging over the steady-state period. The benchmark simulation (black solid line in Fig. 3a) shows a strong convective precipitation maximum reaching around 49 mm h^{-1} but very weak precipitation in the stratiform region. The peak of the precipitation is located 24.6 km behind the gust front. The 200-m resolution simulations are less sensitive to the numerical advection schemes used. The 200-m ODD5 + TKE, 200-m EVEN6(0.04) + TKE, and our 200-m WENO5 + TKE benchmark simulations show similar squall-line structure (Figs. 2b,d,f) and steady-state precipitation distribution (Fig. 3). In addition, the simulated squall lines

TABLE 1. The numerical simulations conducted in this study. The name EVEN6(β) + TKE suggests the sixth-order advection scheme with an artificial dissipation parameter β and TKE-1.5 as the subgrid turbulence model. Other names follow the same format.

Experiment name	Advection scheme	SGS model	Grid spacing Δx (km)	Dissipation parameter β
WENO5 + TKE	Fifth-order WENO	TKE-1.5	0.2, 1, 4	—
ODD5 + TKE	Fifth-order	TKE-1.5	0.2, 1, 4	—
EVEN6(β) + TKE	Sixth-order	TKE-1.5	0.2	0, 0.02, 0.04, 0.24
			1	0, 0.02, 0.04, 0.08, 0.24
			4	0, 0.02, 0.04, 0.08, 0.24
WENO5 + DRM0	Fifth-order WENO	Level 0 DRM	1, 4	—
WENO5 + DRM2	Fifth-order WENO	Level 2 DRM	1, 4	—
ODD5 + DRM0	Fifth-order	Level 0 DRM	1, 4	—
ODD5 + DRM2	Fifth-order	Level 2 DRM	1, 4	—

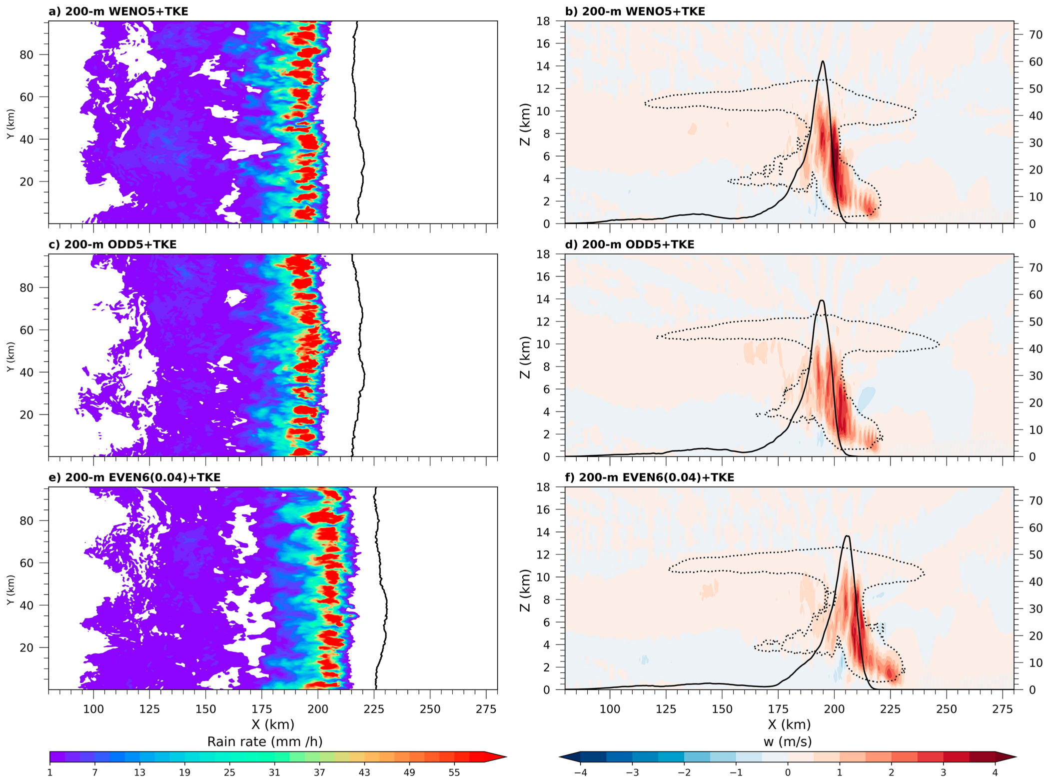

FIG. 2. Instantaneous fields (at 6 h) of 200-m-resolution simulations using (a),(b) WENO5, (c),(d) ODD5, and (e),(f) EVEN6(0.04). (a),(c)(e) Instantaneous rain rate (mm h^{-1}) (shaded) and the surface cold pool leading edge (black solid line). (b),(d),(f) The line-averaged (y) vertical velocity w (m s^{-1}) (shaded), cloud boundaries (black dotted contour lines of 1×10^{-4} mixing ratio of cloud water and ice $q_i + q_c$), and the instantaneous precipitation distribution (black solid lines; with the axis on the right). All simulations use TKE as the turbulence model.

propagate to nearly the same location by the end of the simulation (Fig. 2), suggesting similar forward motions. The 200-m simulations are also not sensitive to the turbulence schemes used (figures not shown).

4. Impact of implicit dissipation

The ODD5 and WENO5 are popular advection schemes in which the numerical dissipation is implicit. In the 200-m LES resolution simulations, the simulated squall lines are less sensitive to the two schemes. In this section, we evaluate the impact of the two advection schemes on squall-line simulations at two gray-zone resolutions, 1 and 4 km. The turbulence model employed in this section is the TKE scheme.

In the 1-km resolution, compared to the WENO5 + TKE simulation, the ODD5 + TKE simulation shows slightly smaller and weaker convective cells (Fig. 4) but a similar precipitation distribution (Fig. 3a). However, in the 4-km resolution, the ODD5 + TKE simulation shows a significantly stronger convective precipitation maximum and weaker stratiform precipitation than the WENO5 + TKE simulation (Figs. 3a and 4). In addition, the 4-km ODD5 + TKE simulation shows much stronger vertical velocities than the 4-km WENO5 + TKE simulation (Figs. 4d,h). Different from WENO5, where the numerical dissipation is enhanced near the sharp gradient to ensure nonoscillatory solutions, ODD5 has lower numerical dissipation near the sharp gradient. These results suggest that 1) the enhanced numerical dissipation near sharp gradients can affect convective updrafts, squall-line structures, and the precipitation distribution and 2) the impact of numerical dissipation on squall-line simulations intensifies with grid size. The underestimation of convective precipitation can also be attributed to the application of the TKE subgrid model at a 4-km resolution, which does not fully resolve the dominant turbulence eddies (Bryan et al. 2003). An additional 4-km resolution simulation using WENO5 + NOSGS (no subgrid mixing scheme) shows enhanced convective precipitation than the WENO5 + TKE, suggesting that the underpredicted convective precipitation in the WENO5 + TKE scheme is also related to the dissipative TKE scheme.

The strength of convective updrafts in the leading edge of cold pools modulates the squall-line structure and the corresponding precipitation distribution. Comparing the 4-km WENO5 + TKE simulation with the 200-m WENO5 + TKE benchmark simulation, the 4-km WENO5 + TKE simulation simulates trailing stratiform clouds that are more concentrated at lower levels (Figs. 2b and 4d). This is because the vertical motions in the 4-km simulation are much weaker,

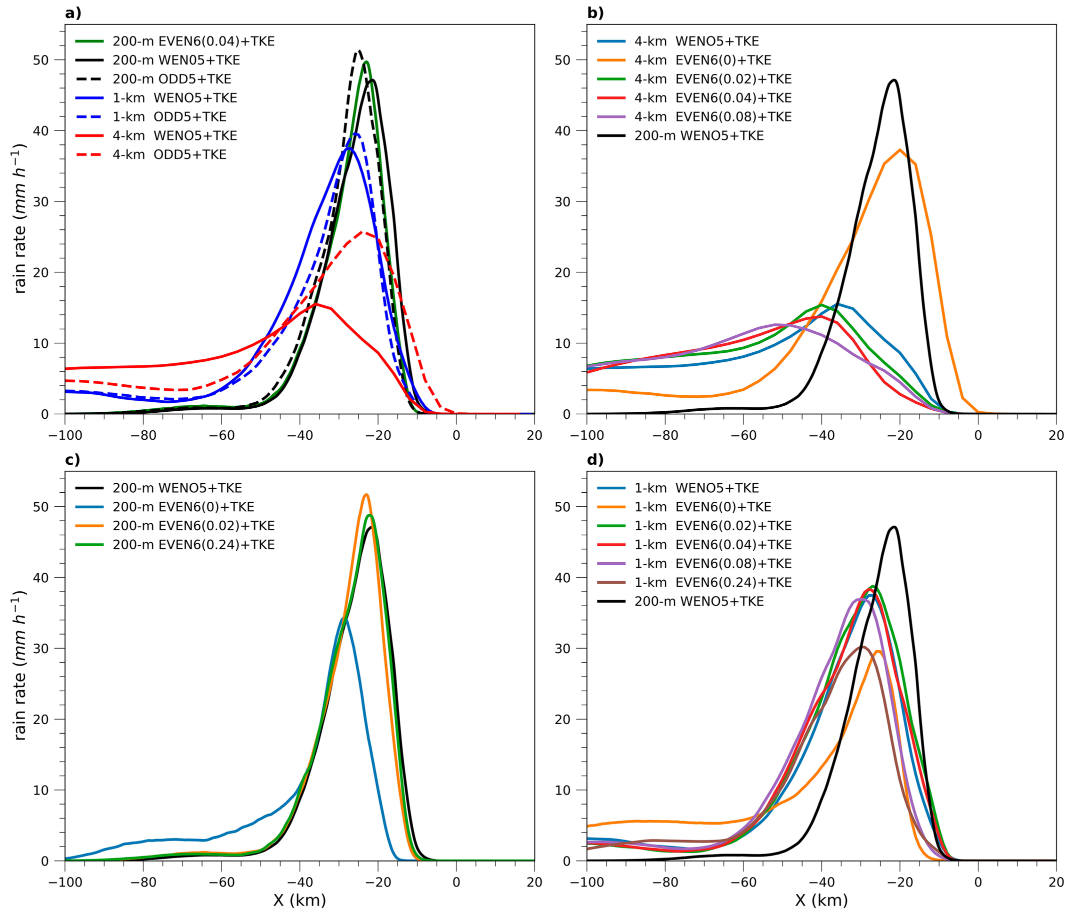

FIG. 3. The line-averaged (y) squall-line steady-state rain rate distribution. The leading edge of the cold pool is normalized to the same location before averaging over the steady-state period. The leading edge of the cold pool is at 0 km. (a) Simulations with resolution $\Delta x = 200$ m, 1 km, and 4 km, using WENO5 (solid lines) and ODD5 (dashed lines) as the advection schemes. (b) The 4-km-resolution simulations and the EVEN6 as the advection scheme with the artificial dissipation parameter $\beta = 0$, 0.02, 0.04, and 0.08. (c) The 200-m-resolution simulations and the EVEN6 as the advection scheme with $\beta = 0$, 0.02, and 0.24. (d) Simulations with resolution 200 m and the EVEN6 as the advection scheme with $\beta = 0$, 0.02, 0.04, 0.08, and 0.24. All simulations use TKE as the turbulence model.

leading to a weaker ascending front-to-rear flow. This weaker ascending front-to-rear flow is not strong enough to bring lower-level moisture to high levels and condenses a greater portion of water at much lower heights. Therefore, the trailing stratiform cloud is developed at relatively low levels. Since the precipitation particles would fall from much lower heights, the decreased exposure time for evaporation increases the volume of precipitation reaching the surface and, therefore, increases precipitation in the trailing stratiform region. Correspondingly, the precipitation distribution of the 4-km WENO5 + TKE simulation shows a much weaker convective precipitation maximum but stronger stratiform precipitation (Fig. 3a). Meanwhile, the precipitation peak for the 4-km WENO5 + TKE simulation is shifted to a location far (35 km) behind the gust front.

The convective precipitation maximum and stratiform precipitation of the 1-km WENO5 + TKE (ODD5 + TKE) simulation are in an intermediary position between the 200-m and 4-km WENO5 + TKE (ODD5 + TKE) simulation. This is because the maximum convective updrafts weaken with grid resolutions (Fig. S1 in the online supplemental material). Previous discussions attribute the stronger convective activities in the 1-km resolution when compared with the 4-km resolution to the enhancement of nonhydrostatic processes (Weisman et al. 1997; Bryan 2012). In this study, we show that the increased numerical dissipation also contributes to this weakening through numerical damping on physical convective updrafts.

5. Impact of explicit dissipation

The comparison of the WENO5 and ODD5 schemes suggests that the degree of numerical dissipation can significantly impact the simulated squall-line structure and corresponding precipitation distribution at the resolution of 4 km, but not at the 1-km and 200-m resolutions. It is therefore important to

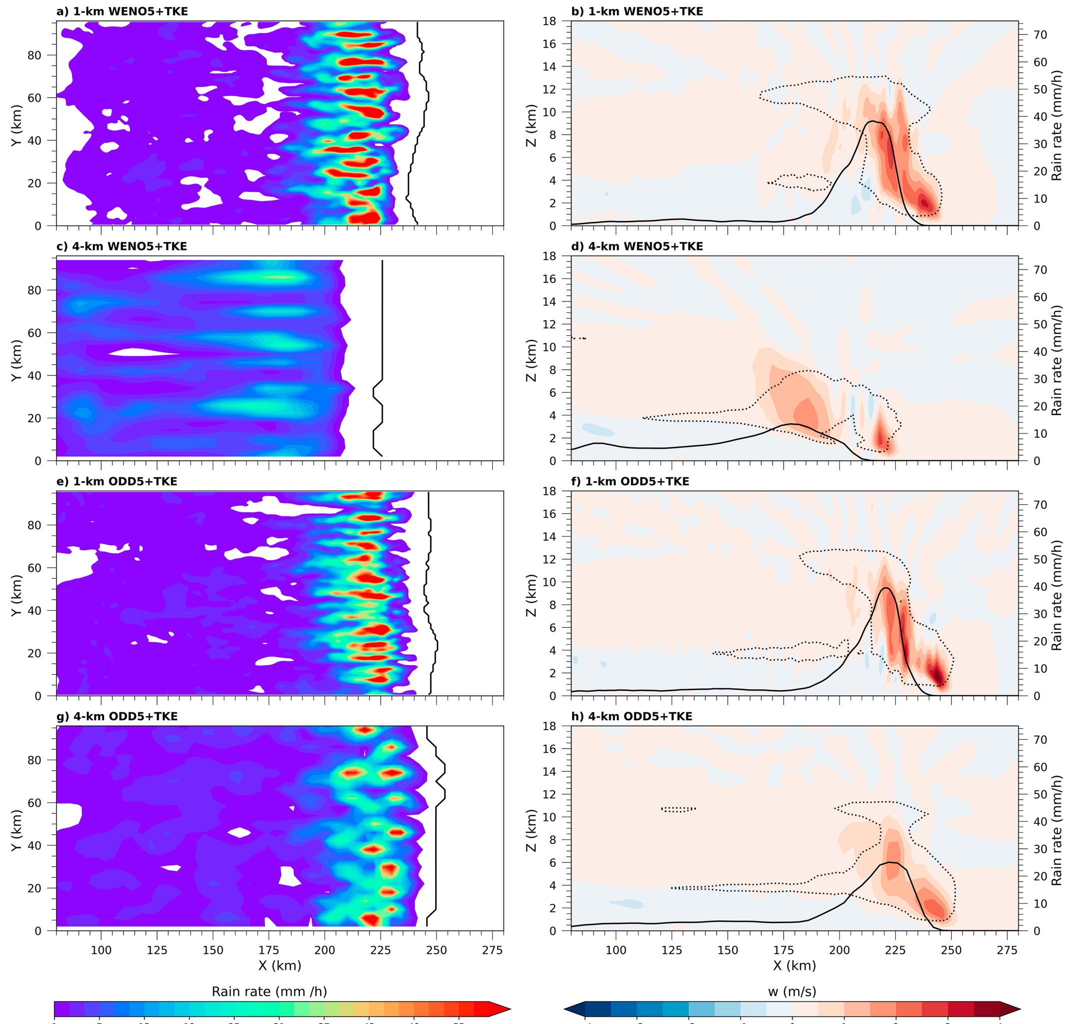

FIG. 4. As in Fig. 2, but showing instantaneous fields (at 6 h) of simulations: (a),(b) 1-km WENO5 + TKE, (c),(d) 4-km WENO5 + TKE, (e),(f) 1-km ODD5 + TKE, and (g),(h) 4-km ODD5 + TKE.

evaluate the impact of numerical dissipation on the squall line at different resolutions. In this section, the centered scheme (EVEN6) in which the numerical dissipation can be controlled by varying explicit artificial dissipation is employed. Here, we will show simulation results in the order of 4-km, 200-m, and 1-km resolution.

a. 4-km resolution simulations

The simulation results of the EVEN6 scheme with artificial dissipation parameters $\beta = 0, 0.02, 0.04, 0.08$, and 0.24 are shown in Fig. 5. Consistent with previous studies (e.g., Weisman et al. 1997), the convective cell size increases with the degree of numerical dissipation (Fig. 5).

The EVEN6 schemes with nonzero explicit dissipation ($\beta = 0.02, 0.04, 0.08, 0.24$) show relatively low stratiform clouds, weak precipitation in the convective region, and stronger precipitation in the stratiform region (Figs. 4d and 5g–i). These results align with the behavior observed in the previously discussed WENO5 + TKE simulation. In addition, the increasing artificial numerical dissipation increasingly slows the squall-line development (Fig. 5). For $\beta = 0.24$ case, the squall line is too slow to evolve into the steady state (Figs. 5e,j). We exclude $\beta = 0.24$ case in the following analysis.

The evolution of mean cold pool intensity (between the cold pool leading edge and 50 km behind the leading edge) is shown in Fig. 6a. The cold pool intensity C is calculated following Bryan and Morrison (2012). In alignment with Weisman et al. (1997), the mean cold pool intensity first weakens, then strengthens, and finally levels off reaching a relatively steady state. The cold pool intensity first decreases because the temperature deficit is reduced as the leading edge of the cold pool starts to mix with ambient air. The afterward strengthening of the cold pool intensity is because the triggered convective cells enhance the cold pool through the evaporation of rainfall and the cold, dry air brought by rainfall-induced downdrafts. The simulations with higher degrees of artificial dissipation show weaker cold pool intensities in the steady state (Fig. 6a). The

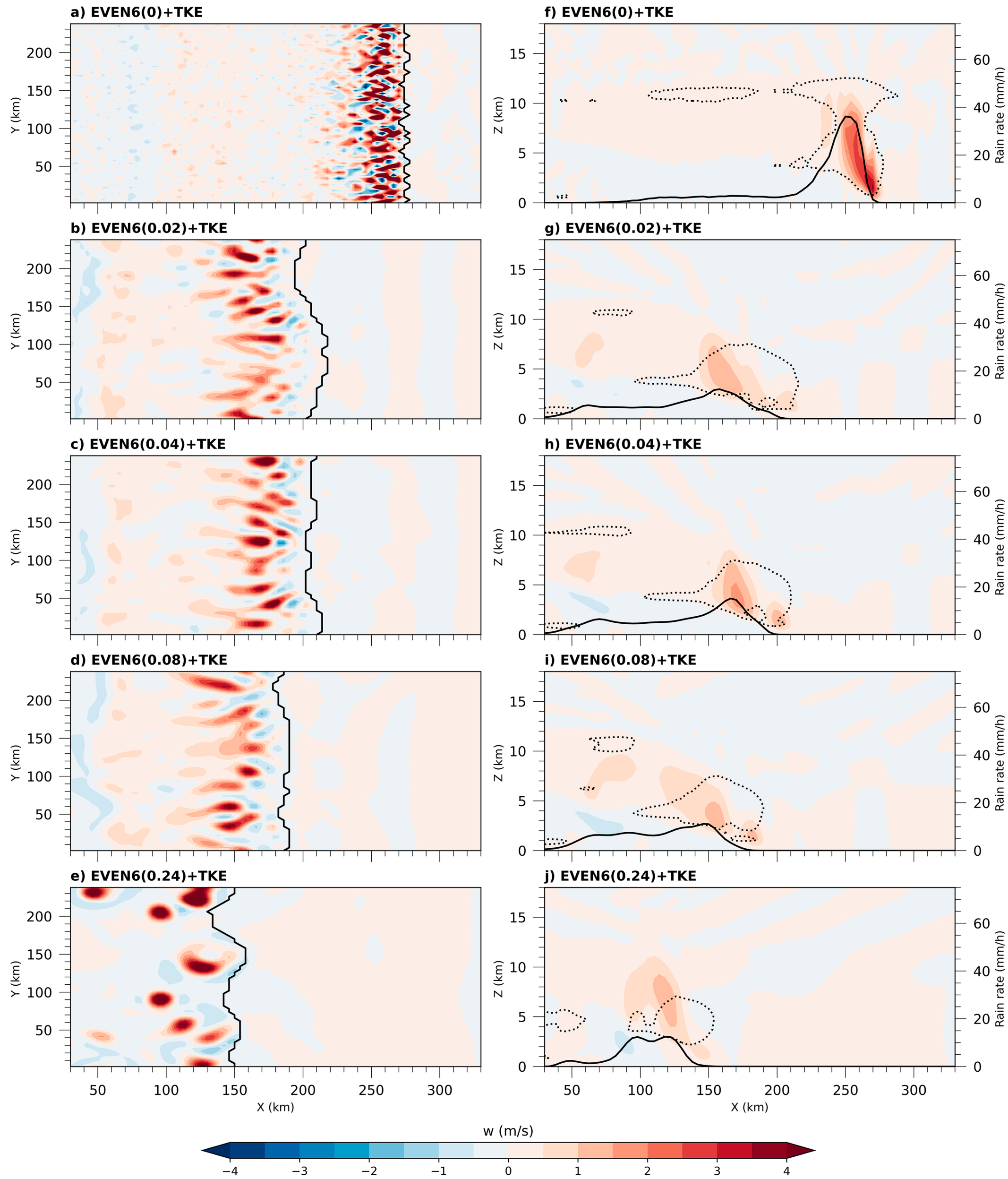

FIG. 5. Instantaneous vertical velocity fields (at the end of hour 6) of 4-km simulations using EVEN6 advection schemes with artificial dissipation parameter β = (a),(f) 0, (b),(g) 0.02, (c),(h) 0.04, (d),(i) 0.24, and (e),(j) 0.24. All simulations use TKE as the turbulence model. (a)–(e) The horizontal slice of vertical velocity at 5-km height and the surface cold pool leading edge (black solid line). (f)–(j) The line-averaged (Y) instantaneous fields. The mixing ratio of cloud water and ice ($q_i + q_c$) (black dotted contour lines) show the cloud boundaries. The black solid line shows the mean precipitation distribution along the squall line with the axis on the right. The shading shows line-averaged vertical velocities w (m s^{-1}).

increase in numerical dissipation slows the triggering of convective cells and weakens convective updrafts, leading to fewer condensates, evaporative cooling, and a weaker cold pool.

The effects of numerical dissipation from the advection scheme are further illustrated by the vertical velocity spectra (Fig. 7a). The computation of the spectra follows methods used in Bryan (2005). The spectra are computed using output in the last 2 h of simulations. According to Skamarock (2004), the optimal spectrum at a coarse resolution would correspond to the high-resolution spectra up to the Nyquist limit of the grid. The 200-m resolution WENO5 simulation spectrum is used as the benchmark spectrum. In the along-squall-line direction, a higher degree of numerical dissipation leads to an increased spectral slope below $6\Delta x$. Compared to the

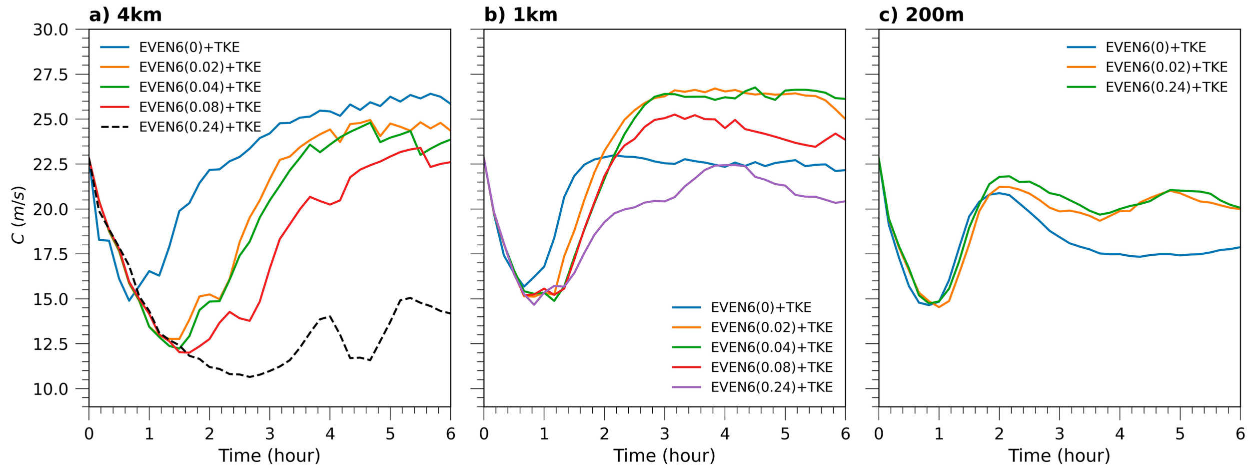

FIG. 6. The evolution of mean cold pool intensity (between the cold pool leading edge and 50 km behind the leading edge) for (a) 4-km, (b) 1-km, and (c) 200-m simulations with varying degrees of explicit dissipation. The cold pool intensity C is calculated following Bryan and Morrison (2012).

benchmark simulation, simulations utilizing advection schemes with explicit numerical dissipation ($\beta = 0.02, 0.04, 0.08$) exhibit weaker energy across all scales. The dominant scale of convective cells is indicated by the wavelength of the energy spectrum peak λ_p (Fig. 7). The empirical numerical dissipation scale λ_d for the sixth-order dissipation is $6\Delta x$ (Durran 2010). The λ_p in the along-squall-line direction closely matches the dissipation scale λ_d, suggesting the direct impact of numerical dissipation on the dominant convective cell. The numerical dissipation from the advection scheme cannot differentiate between the physical oscillations and computational noise. In the 4-km simulations, the numerical dissipation damps physical convective updrafts significantly and further affects the squall-line structure.

For $\beta = 0$ (hereafter, no dissipation) case, where no numerical dissipation is imposed on the convective updrafts, the squall line exhibits significantly stronger updrafts (Fig. 5a) and enhanced precipitation in the convective region (Fig. 3b). This is accompanied by reduced precipitation in the trailing stratiform region, resulting in a precipitation distribution that more closely aligns with the benchmark (Fig. 3b). The strong convective updrafts observed in the no-dissipation case are closely linked to the intensified cold pool strength (Fig. 6a). In terms of the vertical velocity spectra, the no-dissipation case shows slightly enhanced turbulent energy compared to the benchmark in the along-squall-line direction and better agreement in the cross-squall-line direction, except for energy buildup near the 8-km Nyquist limit (Fig. S2).

b. 200-m resolution simulations

The simulation results of the EVEN6 scheme with artificial dissipation parameter $\beta = 0.02, 0.24$ are shown in Fig. 8. The impact of the explicit numerical dissipation decreases with

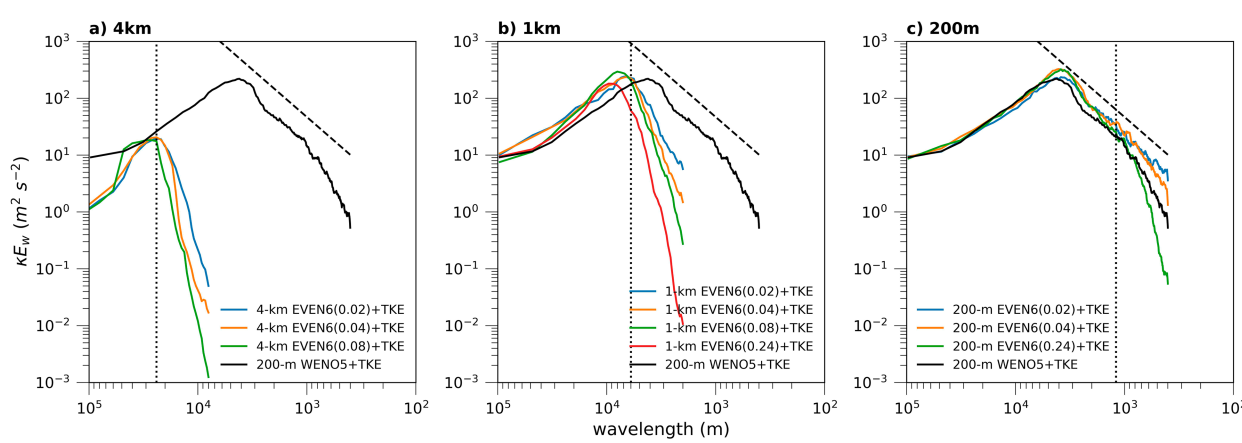

FIG. 7. One-dimensional vertical velocity (along the squall-line direction, at 5 km above the surface) spectra of simulations with grid resolutions of (a) 4 km, (b) 1 km, and (c) 200 m. The simulations use the EVEN6 schemes with varying artificial dissipation parameters β. The spectrum of the 200-m WENO + TKE benchmark simulation is plotted for reference. The black dashed line indicates $k^{-5/3}$ spectrum. The vertical black dotted line indicates $6\Delta x$ which is the empirical numerical dissipation scale λ_d for numerical advection schemes with sixth-order dissipation (Durran 2010).

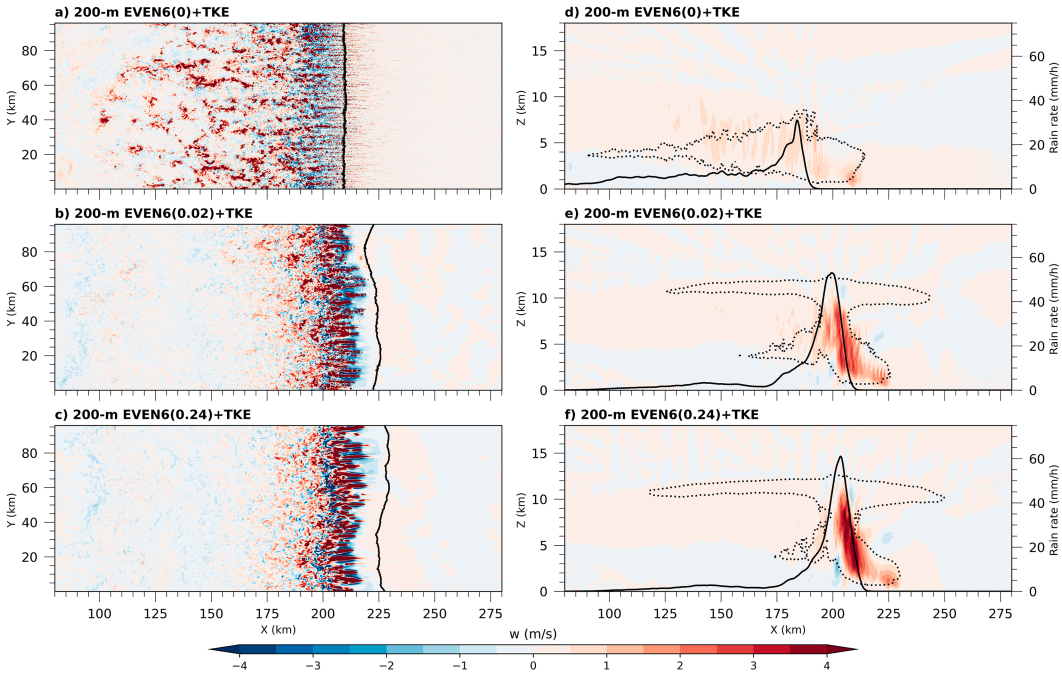

FIG. 8. As in Fig. 5, but showing the 200-m simulations using EVEN6 advection schemes with the artificial dissipation parameter β = (a),(d) 0, (b),(e) 0.02, and (c),(f) 0.24.

increasing grid resolution. This is consistent with the speculation brought by Bryan et al. (2006) that the impact of numerical dissipation should decrease with the increasing resolution because the dissipation will not act directly on the scale of convective cells at high-resolution simulations. The λ_p in the along-squall-line direction is 4 km which is larger than the dissipation scale λ_d of 1.2 km indicated by the vertical black line in Fig. 7c. Therefore, the numerical dissipation from the advection scheme can hardly damp the dominant convective cells.

The evolution of mean cold pool intensity (between the cold pool leading edge and 50 km behind the leading edge) is shown in Fig. 5c. It is worth noting that the 4-km simulations have stronger cold pool intensity compared to the 200-m simulations. However, the 4-km simulations [e.g., EVEN6(0.02) + TKE] have lower maximum convective precipitation and weaker convective updrafts than the corresponding 200-m simulations. For simulations with the same grid resolution, the stronger cold pool intensity corresponds to stronger convective updrafts and a larger convective precipitation maximum. However, this relationship breaks among simulations employing varying grid resolutions probably because the coarser grids cannot resolve the fine-scale processes critical for strong convective updrafts.

In the 200-m resolution simulations, numerical dissipation is necessary. Without the explicitly added numerical dissipation, spurious artificial convection is generated (Fig. 8a). Different from the 4-km simulations, the no-dissipation case in the 200-m simulation shows weak convective updrafts, trailing clouds concentrated at low height levels, underestimated precipitation in the convective region, and overestimated precipitation in the trailing region (Figs. 3c and 8d). Here, we show that very spurious numerical oscillations weaken convective updrafts probably due to increased entrainment. The increased entrainment can directly suppress convective updrafts by diluting moisture concentration, which reduces the positive buoyancy generated through condensation. The degree of entrainment is indirectly quantified by the spatial and temporal average of maximum buoyancy within updrafts because the entrainment is inversely related to the buoyancy within updrafts (e.g., Xu et al. 2021). The spatial averaging is performed over the region extending from the leading edge of the cold pool to 50 km behind it, while the temporal averaging is conducted over the steady-state period. Updrafts are defined as regions where the vertical velocity exceeds 0 m s^{-1}. The spatial and temporal average of the maximum buoyancy within updrafts is 0.163 (m s^{-2}) in the no-dissipation case, significantly smaller than 0.244 (m s^{-2}) in the EVEN6(0.02) + TKE case and 0.248 (m s^{-2}) in the EVEN6(0.24) + TKE case, indicating the increased entrainment in the no-dissipation environment. In the steady state, the no-dissipation case shows the weakest cold pool intensity (Fig. 6c).

c. 1-km resolution simulations

The 200-m and 4-km simulations represent two extremes. The numerical dissipation acts more on physically realistic convective cells in the 4-km simulation, while it acts more on numerical spurious oscillations in the 200-m simulations. In the 1-km simulations, although convective cells are partly damped, the role of numerical dissipation in damping unphysical numerical oscillations is indispensable. The 1-km simulation has shown

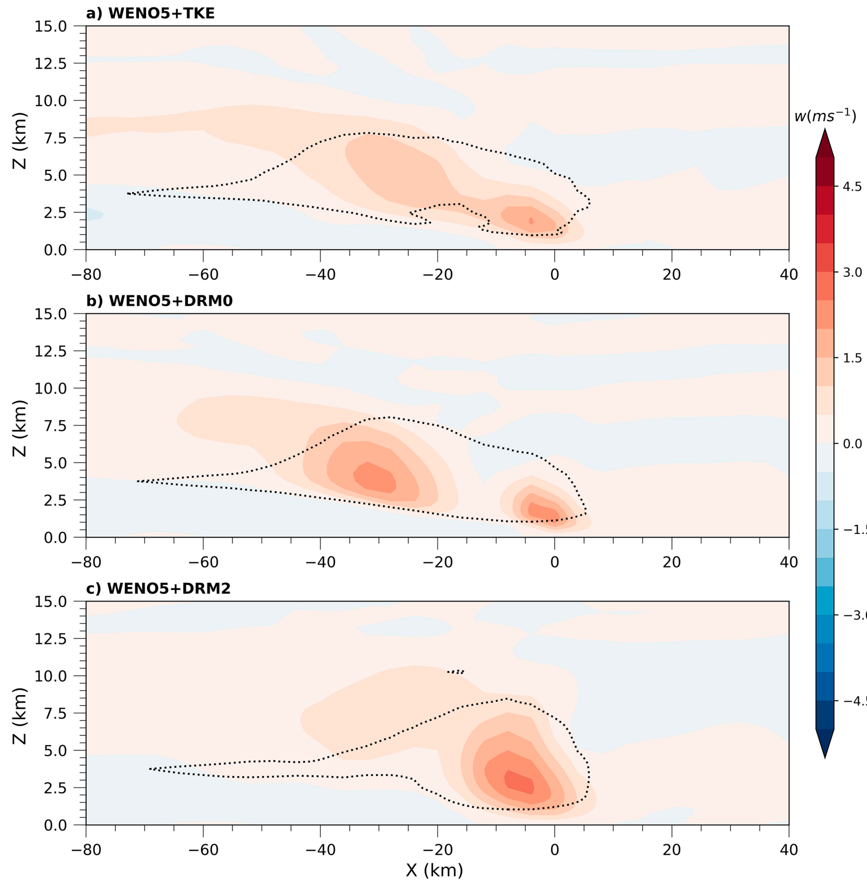

FIG. 9. The along-squall-line averaged vertical velocity w (m s^{-1}) during the steady-state period (last 2 h of simulations) for 4-km (a) WENO5 + TKE, (b) WENO5 + DRM0, and (c) WENO5 + DRM2 simulations. The leading edge of the cold pool is normalized to the same location before averaging over the steady-state period. The black dotted contour lines indicate the cloud boundaries using $q_i + q_c$ threshold of 1×10^{-4}.

similar results to the 200-m simulation (Fig. S3). Compared to the cases with nonzero artificial dissipation, the no-dissipation simulation shows underestimated convective updrafts and underdeveloped high-level trailing stratiform cloud. The excessive entrainment and mixing from spurious numerical oscillations weaken the convective updrafts.

Different from the 200-m simulations, the dominant convective cells in the 1-km simulations are partly damped. The partly damped signal can be seen from the energy spectra (Fig. 7b). The λ_p in the 1-km simulations varies considerably with the degree of numerical dissipation. The increased numerical dissipation increases the cell sizes, subsequently increasing λ_p. In the 200-m simulations, the damping acts primarily on numerical oscillations. Increasing the degree of numerical dissipation only increases the spectral slope below $6\Delta x$ (Fig. 7c).

6. The dynamic reconstruction method

The numerical dissipation, which arises from truncation errors in grid discretization, can greatly impact the squall-line structure and precipitation distribution. Compared to traditional LES closures, the DRM allows turbulence backscatter and reduces the numerical errors from grid discretization (Gullbrand and Chow 2003). Therefore, how the physical mixing from DRM interacts with numerical dissipation from the advection scheme is worthy of further exploration. This section evaluates the performance of DRM in two gray-zone resolutions with WENO5 and ODD5 advection schemes.

a. *4-km resolution simulations*

1) COMBINATION WITH FIFTH-ORDER WENO SCHEME

The combination of the WENO5 advection scheme with the traditional TKE (WENO5 + TKE) has shown significant underestimations of the convective precipitation maximum and overestimations of stratiform precipitation in the 4-km simulations because the numerical dissipation from the WENO5 scheme damps physical convective cells significantly. The use of DRM2 or DRM0, in replacement of TKE, shows enhanced convective updrafts (Fig. 9). The DRM2, in particular, improves the precipitation distribution in terms of increasing

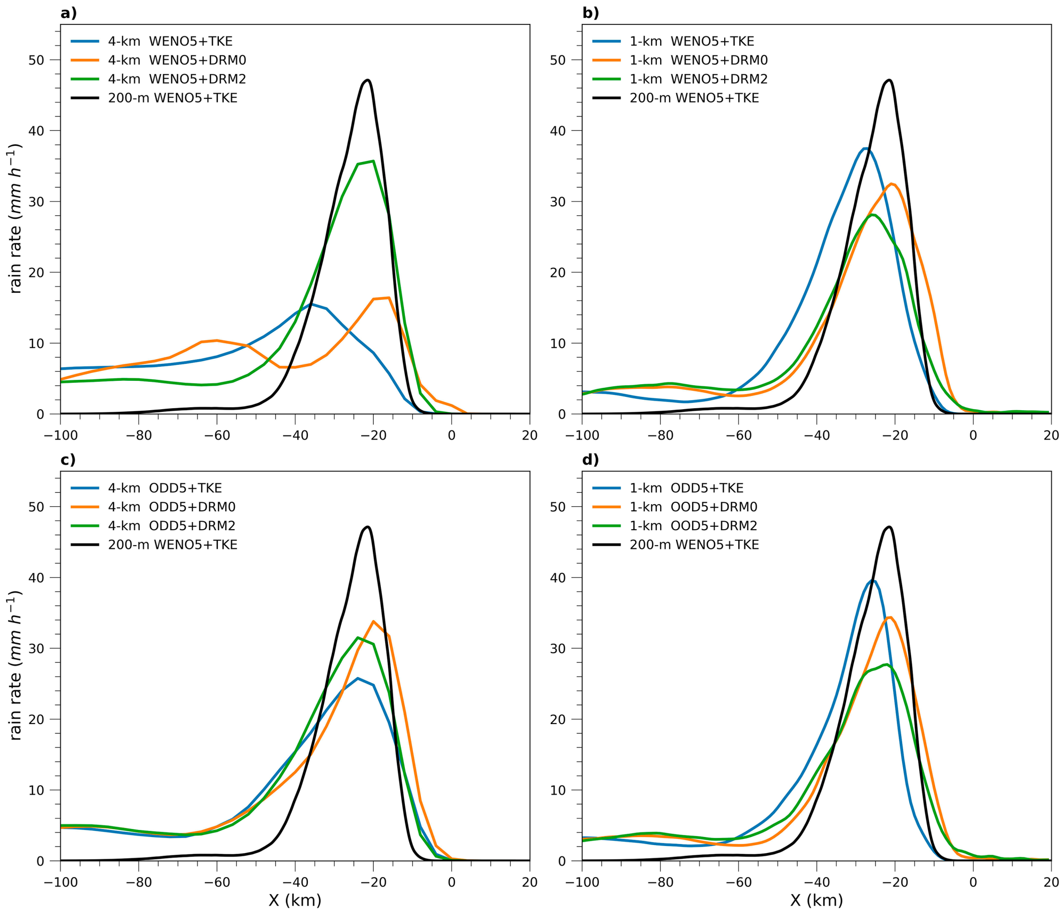

FIG. 10. The along-squall-line averaged steady-state rain rate distribution. As in Fig. 3, but shows results for (a) 4-km resolution simulations using the WENO5 as the advection scheme and the DRM0 and DRM2 as the turbulence model, (b) 1-km resolution simulation using the WENO5 as the advection scheme and DRM0 and DRM2 as the turbulence model, (c) 4-km resolution simulations using the WENO5 as the advection scheme and the DRM0 and DRM2 as the turbulence model, and (d) 1-km resolution simulations using the ODD5 as the advection scheme and the DRM0 and DRM2 as the turbulence model. For easy comparison in single plots, the simulations previously shown in Fig. 3 are also included.

the underestimated convective precipitation maximum, reducing the excessive stratiform precipitation, and simulating the peak precipitation location relative to the cold pool edge (Fig. 10a). The DRM0 shows unsatisfying results in which the convective precipitation maximum is severely underestimated (Fig. 10a). However, there are still signs of improvement in the location of peak precipitation. The DRM0 shifts the convective precipitation peak to a location that is closer to the gust front, which is in better agreement with the benchmark simulation (Fig. 10a).

The improvement of DRM on squall-line simulation is further investigated by quantifying dissipation (or backscatter) on resolved kinetic energy (KE) from the numerical advection scheme and DRM. The implicit dissipation ε on KE from the WENO5 is quantified following Eqs. (7) and (8) in Bryan and Rotunno (2014). The KE dissipation from DRM is quantified by $\Pi = -\tau_{ij}\overline{S}_{ij}$, where τ_{ij} is calculated from Eq. (4). A positive (negative) Π suggests a downgradient (countergradient) transfer of KE from the SFS to resolved scales. In particular, we focus on Π and ε in the vertical direction (Π_v and ε_v) because of their direct impacts on convection. Figure 11 shows along-squall-line averaged steady-state Π_v, ε_v, and $\Pi_v + \varepsilon_v$ for WENO5 + DRM0 and WENO5 + DRM2. The ε_v shows the maximum at the cloud center suggesting the impact of numerical dissipation on convective cells. Compared to WENO5 + DRM0, the WENO5 + DRM2 shows a strong backscatter (negative Π_v in Figs. 11a,d) of vertical KE (KE in the vertical direction) at the top boundary of the cold pool leading edge. Notably, although DRM2 and DRM0 show the downgradient transfer of vertical KE at the upper part of the cloud center (Figs. 11a,d), the backscatter exists in these regions. The net backscatter at the top of the cold pool leading edge results in stronger convective updrafts and counters the numerical dissipation effects imposed on convective cells at upper levels (Figs. 11c,f). The Π and ε, encompassing both horizontal and vertical components, exhibit similar patterns to Π_v and ε_v,

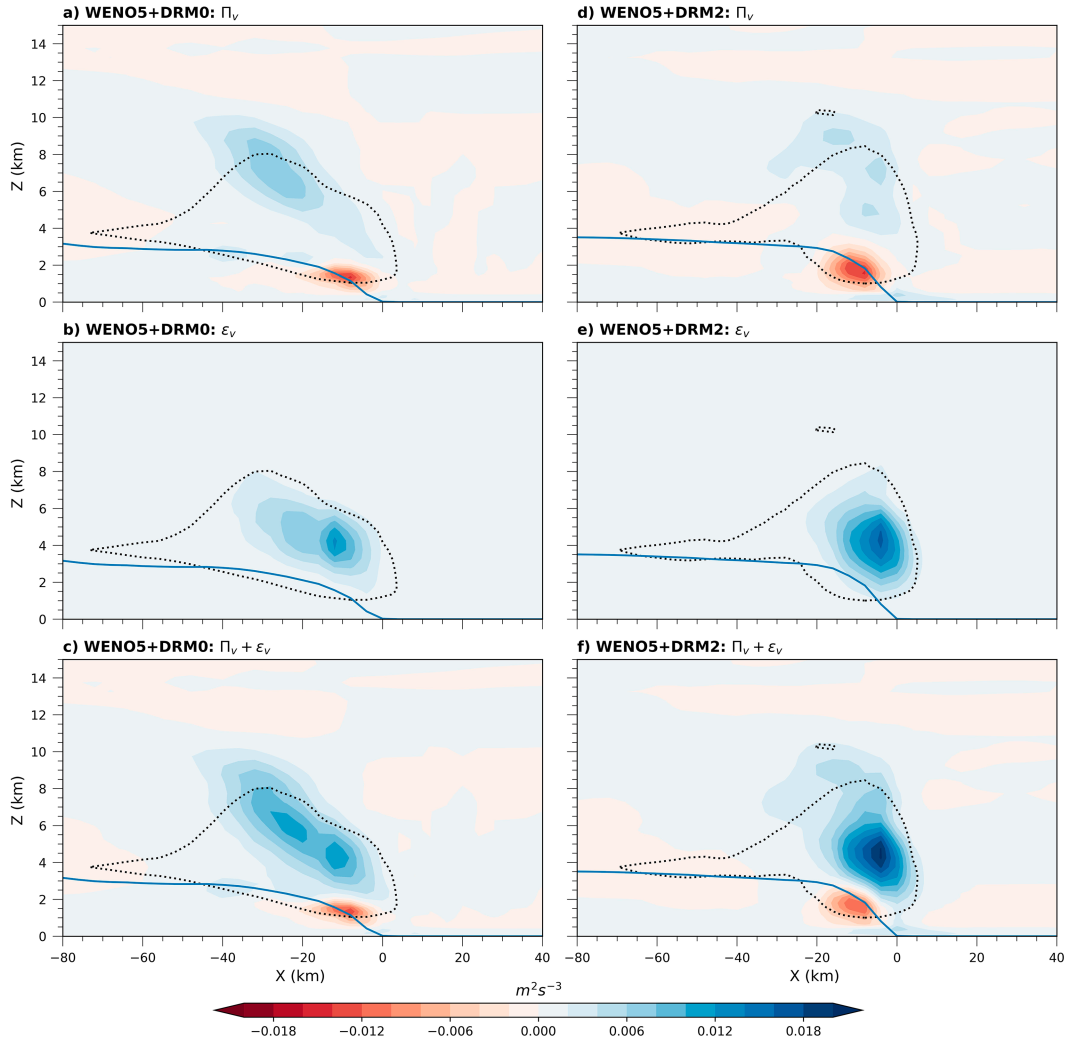

FIG. 11. The along-squall-line averaged steady-state Π_v, ε_v, and $\Pi_v + \varepsilon_v$ for 4-km (a)–(c) WENO5 + DRM0 and (d)–(f) WENO5 + DRM2 simulations. The leading edge of the cold pool is normalized to the same location before averaging over the steady-state period. The black dotted contour lines indicate the cloud boundaries using $q_i + q_c$ threshold of 1×10^{-4}. The blue solid line indicates the cold-pool height that is defined at the height where the buoyancy B first exceeds -0.01 m s^{-2}.

with the exception of a dissipation center located near the surface of the cold pool leading edge (Fig. S4).

Besides the KE transfer, the transfer of potential temperature θ between resolved and SFS is also important because it determines the buoyancy budget (Shi et al. 2018b). The transfer of θ is quantified by $\Pi_\theta = -\tau_{\theta j}\partial\overline{\theta}/\partial x_j$, where $\tau_{\theta j}$ in DRM is calculated from Eq. (5). A positive Π_θ represents the downgradient transport of potential temperature from the resolved scale to SFS, which smooths the resolved field and reduces buoyancy. In contrast, a negative Π_θ indicates a backscatter of potential temperature, which acts to increase buoyancy. In the viscosity-based turbulence model, $\tau_{\theta j}$ is derived from Eq. (2). The transport of θ is always downgradient because $\Pi_\theta = K_m(\partial\overline{\theta}/\partial x_j)^2 \geq 0$. Given that convection occurs in the vertical direction, our analysis focuses on the vertical component $\Pi_{\theta v}$. The WENO5 + DRM2 (WENO5 + DRM0) shows enhanced backscatter of θ at two regions: 1) the top of the leading edge of the cold pool and 2) the midtroposphere within convective clouds (Fig. 12). Compared to WENO5 + DRM0, the backscatter in WENO5 + DRM2 is significantly stronger, and the cold pool height is higher near the leading edge of the cold pool. The larger backscatter of θ near the top of the leading edge of the cold pool in WENO5 + DRM2 increases θ gradients more and allows for a deeper (Fig. 12) and stronger cold pool (Fig. 13a). The stronger cold pool then triggers stronger convective updrafts. However, it is important to note that in the 4-km WENO5 + TKE simulation, the cold pool intensity is stronger than in the 200-m benchmark simulation, yet the convective precipitation is weaker. In the 4-km WENO5 + DRM2 simulations, the cold pool intensity is further overestimated, leading to stronger convective precipitation that more closely approximates the benchmark precipitation. In

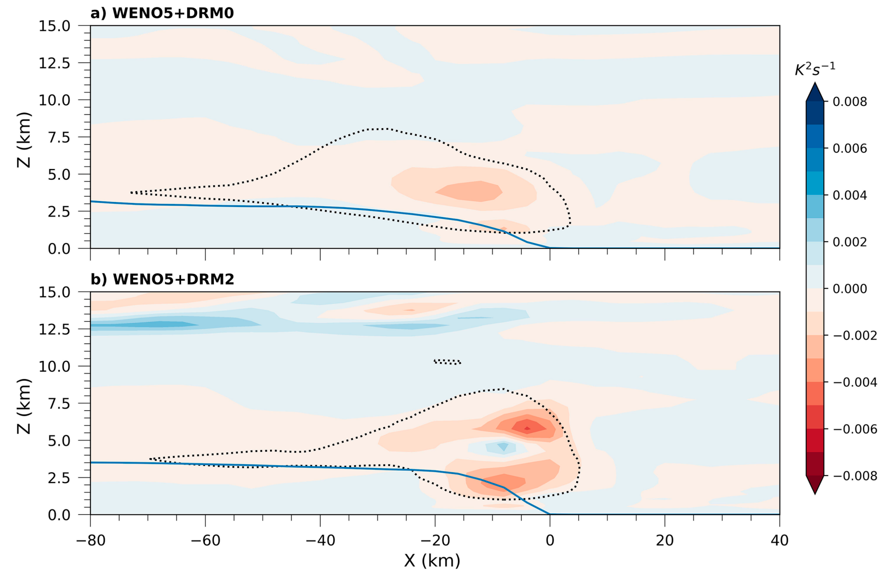

FIG. 12. The along-squall-line averaged steady-state $\Pi_{\theta v}$ for 4-km (a) WENO5 + DRM0 and (b) WENO5 + DRM2 simulations. The leading edge of the cold pool is normalized to the same location before averaging over the steady-state period. The black dotted contour lines indicate the cloud boundaries using $q_i + q_c$ threshold of 1×10^{-4}. The blue solid line indicates the cold pool height that is defined at the height where the buoyancy B first exceeds -0.01 m s^{-2}.

addition to the overestimated cold pool intensity in the 4-km DRM simulations, another compensating error is from environmental entrainment. The environmental entrainment can also affect updraft strength, which in turn affects the convective precipitation. The spatial and temporal mean of the maximum buoyancy within updrafts is 0.238 (m s^{-2}) in the 200-m benchmark simulation, 0.267 (m s^{-2}) in the 4-km WENO5 + TKE simulation, and 0.279 (m s^{-2}) in the 4-km WENO5 + DRM2 simulation, indicating that the entrainment is further underestimated in the 4-km WENO5 + DRM2 simulations. This further underestimation of entrainment can lead to stronger convective updrafts and subsequently enhanced convective precipitation.

The better performance of DRM2 can be seen from the vertical velocity spectra in the midlevel (Fig. 14a). In the along-squall-line direction, the DRMs (DRM0 and DRM2) show more resolved energy than the TKE scheme. DRM2 resolves more energy at large scales than DRM0. The resolved energy of DRM2 is slightly overestimated but is in closer

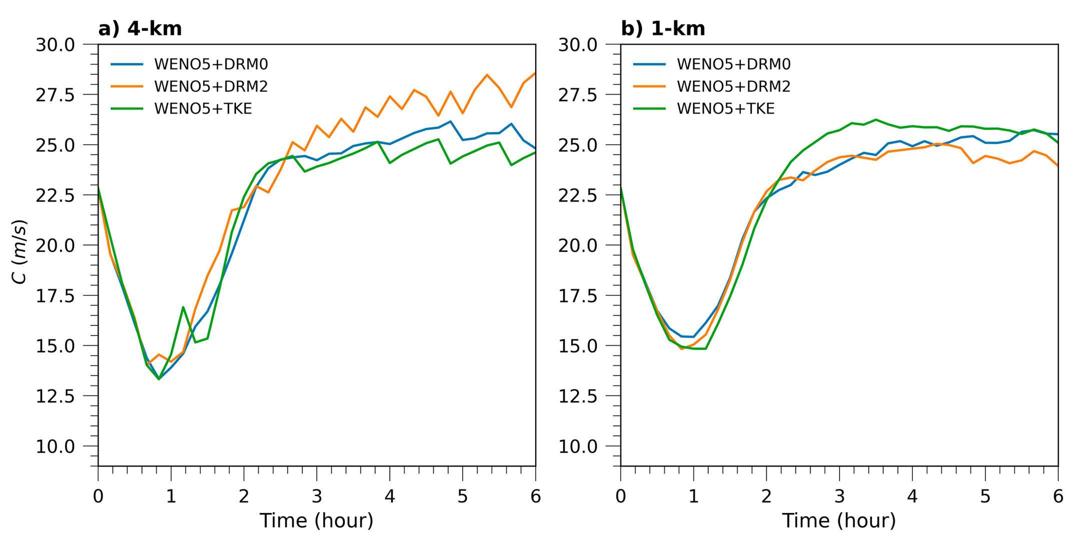

FIG. 13. The evolution of mean cold pool intensity (between the cold pool leading edge and 50 km behind the leading edge) for WENO5 + TKE, WENO5 + DRM0, and WENO5 + DRM2 simulations with a horizontal grid size of (a) 4 and (b) 1 km.

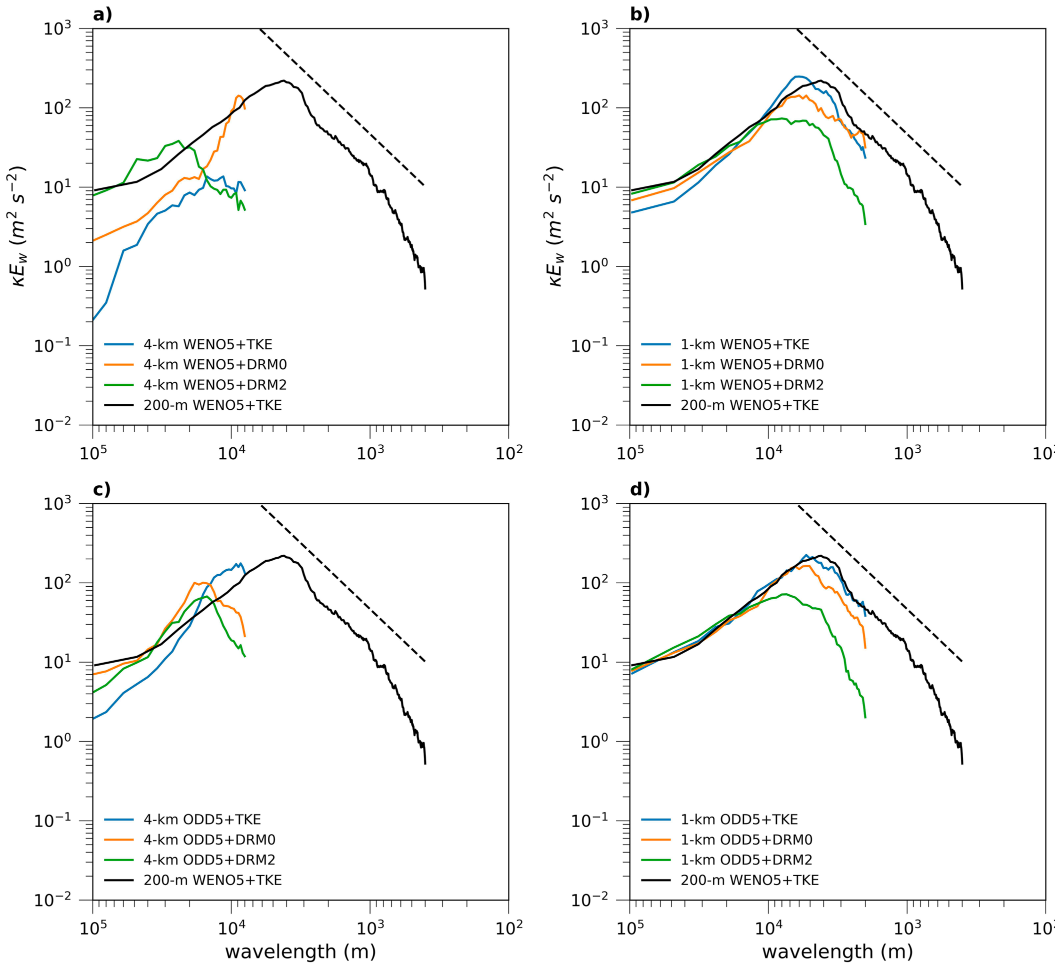

FIG. 14. One-dimensional vertical velocity (along squall-line direction, at 5 km above the surface) spectra of simulations with horizontal grid resolutions of 1 and 4 km. (a) The spectra of 4-km simulations of WENO5 + TKE, EVEN6(0) + TKE, WENO5 + DRM0, and WENO5 + DRM2. (b) As in (a), but for 1-km simulations. (c) The spectra of 4-km simulations of ODD5 + TKE, EVEN6(0) + TKE, ODD5 + DRM0, and ODD5 + DRM2. (d) As in (c), but for 1-km simulations. The spectrum of the 200-m benchmark simulation is plotted for reference. The black dashed line indicates $k^{-5/3}$ spectrum.

agreement with the benchmark simulation spectrum at large scales. At smaller scales, the DRM2 shows a decreasing energy trend with smaller wavelengths, suggesting that small-scale energy is dissipated. DRM0, in contrast, shows an increasing energy trend with smaller wavelengths. The small-scale motions are not well dissipated in DRM0.

2) Combination with fifth-order scheme

The DRMs are also combined with the ODD5 advection scheme. Compared with the traditional TKE, both DRM0 and DRM2 have shown enhancement in convective precipitation maximum (Fig. 10c). The DRM0 shows a slightly stronger convective precipitation maximum (Fig. 10c) and resolved energy than the DRM2 (Fig. 14c). These results are in contrast with the WENO5 simulations where DRM2 simulates a stronger convective precipitation maximum, implying that the optimal combination of the advection scheme and the level of DRM may warrant further investigation. However, we need to stress that the difference in convective precipitation between DRM2 and DRM0 is small and may be due to a slight forward-located peak in DRM2.

b. *1-km resolution simulations*

Based on previous discussions in section 5, the numerical dissipation from the advection schemes is indispensable in the 1-km simulations. Otherwise, spurious numerical oscillations are generated and weaken the convective updrafts by increasing entrainment. On the contrary to the 4-km simulations, both DRM0 and DRM2 show weaker convective precipitation maximum than the traditional TKE model regardless of its combination with the WENO5 or ODD5 advection scheme (Figs. 10b,d). The convective precipitation maximum in the DRMs is underestimated, while the stratiform precipitation is overestimated (Figs. 10b,d). In addition, the high-level

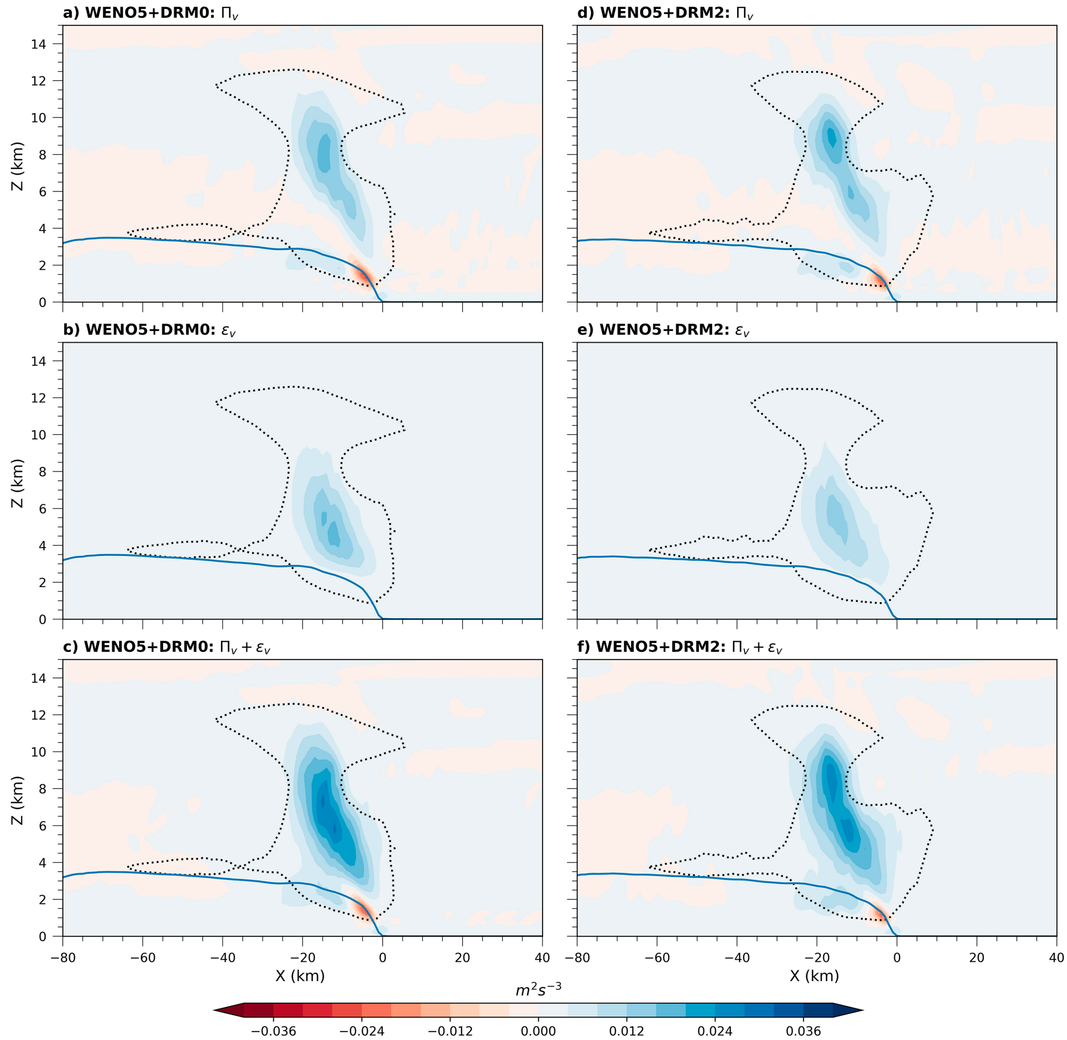

FIG. 15. As in Fig. 11, but for 1-km (a)–(c) WENO5 + DRM0 and (d)–(f) WENO5 + DRM2 simulations.

DRM2 shows a weaker convective precipitation maximum than DRM0.

For the 1-km WENO5 + DRM0 and WENO5 + DRM2 simulations, Π_v and $\Pi_{\theta v}$ during the steady state period are investigated. As with the 4-km simulations, the strongest backscatter of vertical KE (negative Π and Π_v) happens near the top of the leading edge of the cold pool (Fig. 15). The backscatter of vertical KE in the 1-km WENO5 + DRM0 (WENO5 + DRM2) is more concentrated and less important than the downgradient transfer (Fig. 15), suggesting the role of backscatter is reduced with increased resolution. Similarly, the backscatter of KE and θ found near the top of the cold pool leading edge is more concentrated (Fig. S5 and Fig. 6). The DRM simulations, however, also show increased spurious convection than the TKE simulations. The increased small-scale convection in WENO5 + DRM0 and WENO5 + DRM2 is illustrated by the instantaneous vertical velocity field (Figs. 16b,c). The WENO5 + DRM2 has a higher degree of spurious oscillations than the WENO5 + DRM0 (Fig. 16). Similarly, the entrainment is indirectly quantified by calculating the spatial and temporal mean of maximum buoyancy within updrafts. The spatial and temporal mean of the maximum buoyancy within updrafts is 0.292 (m s^{-2}) in 1-km WENO5 + TKE, 0.284 (m s^{-2}) in 1-km WENO5 + DRM0, and 0.277 (m s^{-2}) in 1-km WENO5 + DRM2, suggesting increased entrainment in the 1-km DRM simulations. As discussed in section 5, the increased entrainment is associated with weaker convective updrafts.

The evolution of mean cold pool intensity for 1-km WENO5 + DRM0, WENO5 + DRM2, and WENO5 + TKE is shown in Fig. 13b. The DRMs show weaker cold pool intensity during the steady-state periods than WENO5 + TKE. In particular, DRM2 shows a weaker cold pool than DRM0. These results suggest that although the backscatter of vertical KE and potential temperature tends to enhance convection and cold pool intensity, the increased occurrence of spurious convection in the DRM simulations has a more significant impact on the intensities of cold pools. The vertical velocity spectra (Figs. 14b,d) also convey the message that the

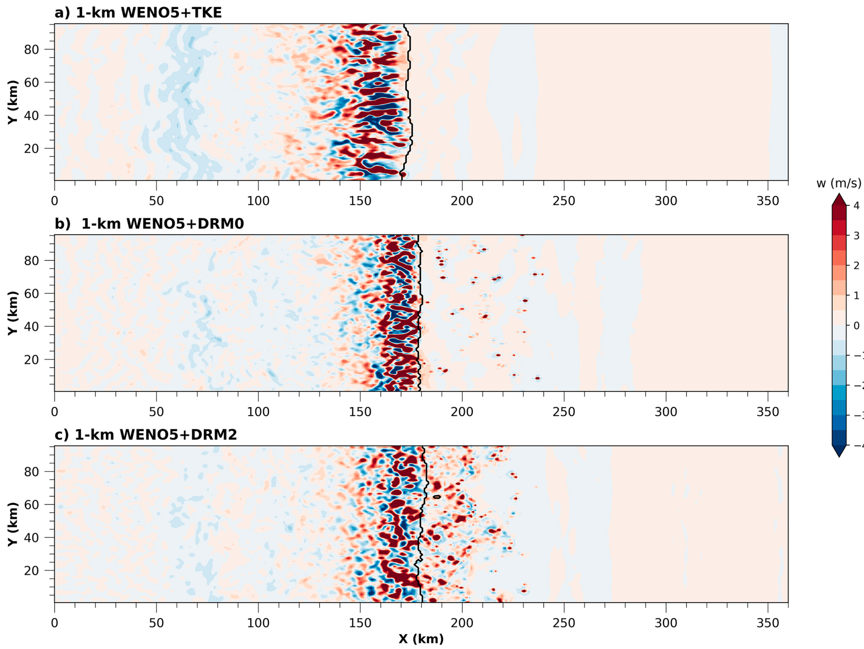

FIG. 16. The vertical velocity of a horizontal plane at a height of 5 km in the 4th h for 1-km resolution simulations: (a) WENO5 + TKE, (b) WENO5 + DRM0, and (c) WENO5 + DRM2. As in Fig. 5, the black solid line indicates the cold pool leading edge.

backscattering DRMs have weaker dominant convective updrafts. The spectra peak that indicates the intensities of energy-containing turbulences is smaller in WENO5 + DRM2 (ODD5 + DRM2) than that in WENO5 + TKE (ODD5 + TKE). The WENO5 + DRM2 (ODD5 + DRM2) has shown an even weaker spectra peak than the WENO5 + DRM0 (ODD5 + DRM0). It is also important to note that the convective cells of the WENO5 + DRM2 or WENO5 + DRM0 simulations are not in a grid scale (Figs. 16b,c). Although the oscillations from the WENO5 + DRM2 and WENO5 + DRM0 simulations are similar to the pattern in EVEN6(0) + TKE, they are indeed different because the oscillations are mostly from the numerical errors in the EVEN6(0) + TKE, while the oscillations are mostly from backscatter of turbulence in the DRM.

7. Conclusions

In this study, we evaluated three numerical advection schemes and investigated the impact of numerical dissipation on squall-line simulations with various grid resolutions (200 m, 1 km, and 4 km). For squall-line simulations, the 200-m grid size falls into the LES resolution range, while the 1- and 4-km grid sizes are at gray-zone resolutions.

The role of numerical dissipation varies across different grid resolutions. At the LES resolution, a sufficient degree of numerical dissipation is necessary because, without it, spurious numerical oscillations may develop into numerous small-scale convective cells. These cells increase entrainment, leading to weaker convective updrafts and reduced convective precipitation. The needed numerical dissipation can be provided by the implicit dissipation of odd-order schemes or by adding artificial numerical dissipation to the even-order schemes. The simulation results are not sensitive to the strength of numerical dissipation at the LES resolution because the numerical dissipation acts primarily on turbulent eddies that are far smaller than the dominant physical convective cells.

In the gray-zone resolution of 4 km, the numerical dissipation damps physical convective cells significantly, and convective updrafts are generally weak. The weaker front-to-rear flows, similarly, produce excessive stratiform precipitation but weaker convective precipitation. Therefore, advection schemes with minimum numerical dissipation are recommended. In the gray-zone resolution of 1 km, although convective cells are also damped, the numerical dissipation in the advection scheme is still important. Without sufficient numerical dissipation, sporadic convections generated from spurious numerical oscillations increase entrainment and weaken convective updrafts.

The dynamic reconstruction model (DRM) is an advanced turbulence closure model that can model both forward- and backscatter of SGS turbulence (Chow et al. 2005), potentially reducing the numerical dissipation effects in advection schemes. In combination with two advection schemes that have implicit numerical dissipation, the DRM is evaluated at two gray-zone resolutions (1 and 4 km). In the gray-zone resolution of 4 km, the application of the DRM can enhance cold pool strength and convective updrafts, reduce the overpredicted stratiform precipitation, and increase the underpredicted convective precipitation maximum. The numerical dissipation at the 4-km resolution damps physical convective updrafts greatly. The ability to model backscatter turbulence in the DRM allows the numerical dissipation effects to be reduced. The DRM shows strong backscatter of kinetic energy and potential temperature along the top boundary of the cold pool leading edge, inducing stronger cold pools and convective updrafts.

In the gray-zone resolution of 1 km, the application of the DRM leads to excessive generation of small-scale convective motions. The DRM cannot simulate a stronger convective precipitation maximum regardless of its combinations with less or more dissipative numerical advection schemes. This is because the increased spurious convections exert more influence on cold pool strength than other factors such as backscatter of kinetic energy and potential temperature near the top boundary of the cold pool leading edge. The 1-km simulations are sensitive to DRM backscatter probably because the grid-scale numerical oscillations are close to the sizes of individual convective cores, which are around 1 km (LeMone and Zipser 1980; Shi et al. 2019), and thereby can easily develop into spurious convection in the unstable environment. Of note, in the LES resolution of 200 m, the application of the DRM does not cause spurious convection although numerical dissipation from the advection scheme is indispensable. This is because the turbulence backscatter in LES is not as important as that in gray-zone simulations (Chow et al. 2019).

This work reveals that numerical dissipation effects from advection schemes vary across different gray-zone resolutions in a squall-line simulation. At the 4-km resolution, numerical dissipation can be detrimental, as it excessively suppresses physical convective cells and distorts the squall-line structure. However, at the 1-km resolution, numerical dissipation is indispensable for maintaining simulation stability, as it effectively damps numerical oscillations and prevents the development of spurious convection, thereby preserving the fidelity of the squall-line structure. The DRM turbulence model assumes subfilter-scale effects include backscatter and reconstructs such effects based on resolved flows. In terms of precipitation distribution, this approach improves the squall-line simulation at the 4-km gray-zone resolution. However, it underperforms at the 1-km gray-zone resolution, where spurious backscatter is found.

Acknowledgments. The work is substantially supported by a grant from the Research Grants Council (RGC) of the Hong Kong Special Administrative Region, China (Project Reference: AoE/P-601/23-N), and the Center for Ocean Research in Hong Kong and Macau (CORE), a joint research center between the Laoshan Laboratory and the Hong Kong University of Science and Technology (HKUST). JC is additionally supported by RGC Grants AoE/E-603/18 and HKUST-16301721. The authors thank the HKUST Fok Ying Tung Research Institute and the National Supercomputing Center in Guangzhou Nansha subcenter for providing high-performance computational resources.

Data availability statement. The CM1 model code and namelist files used to produce the simulations in this study are available at https://github.com/JiananChenUST/DRMCM1.

REFERENCES

Arakawa, A., and V. R. Lamb, 1977: Computational design of the basic dynamical processes of the UCLA general circulation model. *General Circulation Models of the Atmosphere*, J. Chang, Ed., Methods in Computational Physics: Advances in Research and Applications, Vol. 17, Elsevier, 173–265.

Beare, R. J., 2014: A length scale defining partially-resolved boundary-layer turbulence simulations. *Bound.-Layer Meteor.*, **151**, 39–55, https://doi.org/10.1007/s10546-013-9881-3.

Borges, R., M. Carmona, B. Costa, and W. S. Don, 2008: An improved weighted essentially non-oscillatory scheme for hyperbolic conservation laws. *J. Comput. Phys.*, **227**, 3191–3211, https://doi.org/10.1016/j.jcp.2007.11.038.

Bryan, G. H., 2005: Spurious convective organization in simulated squall lines owing to moist absolutely unstable layers. *Mon. Wea. Rev.*, **133**, 1978–1997, https://doi.org/10.1175/MWR2952.1.

——, 2012: Effects of surface exchange coefficients and turbulence length scales on the intensity and structure of numerically simulated hurricanes. *Mon. Wea. Rev.*, **140**, 1125–1143, https://doi.org/10.1175/MWR-D-11-00231.1.

——, and J. M. Fritsch, 2002: A benchmark simulation for moist nonhydrostatic numerical models. *Mon. Wea. Rev.*, **130**, 2917–2928, https://doi.org/10.1175/1520-0493(2002)130<2917:ABSFMN>2.0.CO;2.

——, and H. Morrison, 2012: Sensitivity of a simulated squall line to horizontal resolution and parameterization of microphysics. *Mon. Wea. Rev.*, **140**, 202–225, https://doi.org/10.1175/MWR-D-11-00046.1.

——, and R. Rotunno, 2014: Gravity currents in confined channels with environmental shear. *J. Atmos. Sci.*, **71**, 1121–1142, https://doi.org/10.1175/JAS-D-13-0157.1.

——, J. C. Wyngaard, and J. M. Fritsch, 2003: Resolution requirements for the simulation of deep moist convection. *Mon. Wea. Rev.*, **131**, 2394–2416, https://doi.org/10.1175/1520-0493(2003)131<2394:RRFTSO>2.0.CO;2.

——, J. C. Knievel, and M. D. Parker, 2006: A multimodel assessment of RKW theory's relevance to squall-line characteristics. *Mon. Wea. Rev.*, **134**, 2772–2792, https://doi.org/10.1175/MWR3226.1.

Chow, F. K., R. L. Street, M. Xue, and J. H. Ferziger, 2005: Explicit filtering and reconstruction turbulence modeling for large-eddy simulation of neutral boundary layer flow. *J. Atmos. Sci.*, **62**, 2058–2077, https://doi.org/10.1175/JAS3456.1.

——, C. Schär, N. Ban, K. A. Lundquist, L. Schlemmer, and X. Shi, 2019: Crossing multiple gray zones in the transition from mesoscale to microscale simulation over complex terrain. *Atmosphere*, **10**, 274, https://doi.org/10.3390/atmos10050274.

Deardorff, J. W., 1980: Stratocumulus-capped mixed layers derived from a three-dimensional model. *Bound.-Layer Meteor.*, **18,** 495–527, https://doi.org/10.1007/BF00119502.

Durran, D. R., 2010: *Numerical Methods for Fluid Dynamics: With Applications to Geophysics.* Texts in Applied Mathematics, Vol. 32, Springer Science & Business Media, 532 pp.

Gullbrand, J., and F. K. Chow, 2003: The effect of numerical errors and turbulence models in large-eddy simulations of channel flow, with and without explicit filtering. *J. Fluid Mech.*, **495**, 323–341, https://doi.org/10.1017/S0022112003006268.

Honnert, R., and Coauthors, 2020: The atmospheric boundary layer and the "gray zone" of turbulence: A critical review. *J. Geophys. Res. Atmos.*, **125**, e2019JD030317, https://doi.org/10.1029/2019JD030317.

Jiang, G.-S., and C.-W. Shu, 1996: Efficient implementation of weighted ENO schemes. *J. Comput. Phys.*, **126**, 202–228, https://doi.org/10.1006/jcph.1996.0130.

Knievel, J. C., G. H. Bryan, and J. P. Hacker, 2007: Explicit numerical diffusion in the WRF model. *Mon. Wea. Rev.*, **135**, 3808–3824, https://doi.org/10.1175/2007MWR2100.1.

Košović, B., D. Muñoz-Esparza, and J. A. Sauer, 2016: Improving spectral resolution of finite difference schemes for multiscale modeling applications using numerical weather prediction model. *22nd Symp. on Boundary Layers and Turbulence*, Salt Lake City, UT, Amer. Meteor. Soc., 3B.5, https://ams.confex.com/ams/32AgF22BLT3BG/webprogram/Paper295892.html.

Kusaka, H., A. Crook, J. C. Knievel, and J. Dudhia, 2005: Sensitivity of the WRF model to advection and diffusion schemes for simulation of heavy rainfall along the Baiu Front. *SOLA*, **1**, 177–180, https://doi.org/10.2151/sola.2005-046.

Lai, K. T., and M. L. Waite, 2020: Resolution dependence and subfilter-scale motions in idealized squall-line simulations. *Mon. Wea. Rev.*, **148**, 3059–3078, https://doi.org/10.1175/MWR-D-19-0330.1.

LeMone, M. A., and E. J. Zipser, 1980: Cumulonimbus vertical velocity events in gate. Part I: Diameter, intensity and mass flux. *J. Atmos. Sci.*, **37**, 2444–2457, https://doi.org/10.1175/1520-0469(1980)037<2444:CVVEIG>2.0.CO;2.

Moeng, C.-H., 1984: A large-eddy-simulation model for the study of planetary boundary-layer turbulence. *J. Atmos. Sci.*, **41**, 2052–2062, https://doi.org/10.1175/1520-0469(1984)041<2052:ALESMF>2.0.CO;2.

Morrison, H., G. Thompson, and V. Tatarskii, 2009: Impact of cloud microphysics on the development of trailing stratiform precipitation in a simulated squall line: Comparison of one- and two-moment schemes. *Mon. Wea. Rev.*, **137**, 991–1007, https://doi.org/10.1175/2008MWR2556.1.

Parodi, A., and S. Tanelli, 2010: Influence of turbulence parameterizations on high-resolution numerical modeling of tropical convection observed during the TC4 field campaign. *J. Geophys. Res.*, **115**, D00J14, https://doi.org/10.1029/2009JD013302.

Pressel, K. G., C. M. Kaul, T. Schneider, Z. Tan, and S. Mishra, 2015: Large-eddy simulation in an anelastic framework with closed water and entropy balances. *J. Adv. Model. Earth Syst.*, **7**, 1425–1456, https://doi.org/10.1002/2015MS000496.

Rotunno, R., J. B. Klemp, and M. L. Weisman, 1988: A theory for strong, long-lived squall lines. J. Atmos. Sci., 45, 463–485, https://doi.org/10.1175/1520-0469(1988)045<0463:ATFSLL>2.0.CO;2.

Shi, X., F. K. Chow, R. L. Street, and G. H. Bryan, 2018a: An evaluation of LES turbulence models for scalar mixing in the stratocumulus-capped boundary layer. *J. Atmos. Sci.*, **75**, 1499–1507, https://doi.org/10.1175/JAS-D-17-0392.1.

——, H. L. Hagen, F. K. Chow, G. H. Bryan, and R. L. Street, 2018b: Large-eddy simulation of the stratocumulus-capped boundary layer with explicit filtering and reconstruction turbulence modeling. *J. Atmos. Sci.*, **75**, 611–637, https://doi.org/10.1175/JAS-D-17-0162.1.

——, F. K. Chow, R. L. Street, and G. H. Bryan, 2019: Key elements of turbulence closures for simulating deep convection at kilometer-scale resolution. *J. Adv. Model. Earth Syst.*, **11**, 818–838, https://doi.org/10.1029/2018MS001446.

Shin, H. H., and S.-Y. Hong, 2015: Representation of the subgrid-scale turbulent transport in convective boundary layers at gray-zone resolutions. *Mon. Wea. Rev.*, **143**, 250–271, https://doi.org/10.1175/MWR-D-14-00116.1.

Simon, J. S., B. Zhou, J. D. Mirocha, and F. K. Chow, 2019: Explicit filtering and reconstruction to reduce grid dependence in convective boundary layer simulations using WRF-LES. *Mon. Wea. Rev.*, **147**, 1805–1821, https://doi.org/10.1175/MWR-D-18-0205.1.

Skamarock, W. C., 2004: Evaluating mesoscale NWP models using kinetic energy spectra. *Mon. Wea. Rev.*, **132**, 3019–3032, https://doi.org/10.1175/MWR2830.1.

——, and Coauthors, 2008: A description of the Advanced Research WRF version 3. NCAR Tech. Note NCAR/TN-475+STR, 113 pp., https://doi.org/10.5065/D68S4MVH.

Stolz, S., and N. A. Adams, 1999: An approximate deconvolution procedure for large-eddy simulation. *Phys. Fluids*, **11**, 1699–1701, https://doi.org/10.1063/1.869867.

Sun, S., B. Zhou, M. Xue, and K. Zhu, 2021: Scale-similarity subgrid-scale turbulence closure for supercell simulations at kilometer-scale resolutions: Comparison against a large-eddy simulation. *J. Atmos. Sci.*, **78**, 417–437, https://doi.org/10.1175/JAS-D-20-0187.1.

Takemi, T., and R. Rotunno, 2003: The effects of subgrid model mixing and numerical filtering in simulations of mesoscale cloud systems. *Mon. Wea. Rev.*, **131**, 2085–2101, https://doi.org/10.1175/1520-0493(2003)131<2085:TEOSMM>2.0.CO;2.

Wang, A., Y. Pan, and P. M. Markowski, 2021: The influence of WENO schemes on large-eddy simulations of a neutral atmospheric boundary layer. *J. Atmos. Sci.*, **78**, 3613–3628, https://doi.org/10.1175/JAS-D-21-0033.1.

Weisman, M. L., and R. Rotunno, 2004: "A theory for strong long-lived squall lines" revisited. *J. Atmos. Sci.*, **61**, 361–382, https://doi.org/10.1175/1520-0469(2004)061<0361:ATFSLS>2.0.CO;2.

——, W. C. Skamarock, and J. B. Klemp, 1997: The resolution dependence of explicitly modeled convective systems. *Mon. Wea. Rev.*, **125**, 527–548, https://doi.org/10.1175/1520-0493(1997)125<0527:TRDOEM>2.0.CO;2.

Wicker, L. J., and W. C. Skamarock, 2002: Time-splitting methods for elastic models using forward time schemes. *Mon. Wea. Rev.*, **130**, 2088–2097, https://doi.org/10.1175/1520-0493(2002)130<2088:TSMFEM>2.0.CO;2.

Wong, V. C., and D. K. Lilly, 1994: A comparison of two dynamic subgrid closure methods for turbulent thermal convection. *Phys. Fluids*, **6**, 1016–1023, https://doi.org/10.1063/1.868335.

Xu, X., C. Sun, C. Lu, Y. Liu, G. J. Zhang, and Q. Chen, 2021: Factors affecting entrainment rate in deep convective clouds and parameterizations. *J. Geophys. Res. Atmos.*, **126**, e2021JD034881, https://doi.org/10.1029/2021JD034881.

Xue, M., 2000: High-order monotonic numerical diffusion and smoothing. *Mon. Wea. Rev.*, **128**, 2853–2864, https://doi.org/10.1175/1520-0493(2000)128<2853:HOMNDA>2.0.CO;2.